Thermodynamics and kinetics of interconversion between platinum nanoparticles and cations in zeolites

Anupama Jayaraman,[1,‡] *Asanka Wijerathne,*[1,‡] *Keka Mandal,*[1] *Rajamani Gounder,*[2] *Christopher Paolucci*[1,*]

[1]Department of Chemical Engineering, University of Virginia, P.O. Box 400259, Charlottesville, Virginia 22903, United States

[2]Charles D. Davidson School of Chemical Engineering, Purdue University, 480 Stadium Mall Drive, West Lafayette, Indiana 47907, United States

Abstract

In metal-containing zeolites, sintering and redispersion processes exercise control over the identity of metal site structures, but the thermodynamic and kinetic factors that influence these molecular-level processes are not completely understood. Here, we assess the ability of first principles informed free energy models (for supported and unsupported nanoparticles) and kinetic models integrating Ostwald ripening with atom trapping to describe the interconversion between Pt cations and nanoparticles encapsulated in chabazite (CHA) zeolites. Density functional theory-derived thermodynamic phase diagrams show that the interconversion between cations, favored in oxidizing environments, and particles, favored in reducing environments, is fully reversible within a wide range of their respective conditions (temperatures and pressures) for CHA and several other zeolite topologies. Kinetic Monte Carlo simulations of Pt redispersion are consistent with experimentally observed redispersion kinetics of encapsulated Pt nanoparticles in CHA zeolites, and model results suggest the zeolite host imparts additional stability for Pt nanoparticles. We envision our thermodynamic and kinetic models for Pt-CHA are also capable of describing nanoparticle and cation interconversions for other zeolite frameworks under similar conditions.

KEYWORDS

Zeolite, Ion-exchange, Encapsulation, Platinum, Kinetic Monte Carlo, Ostwald Ripening

Graphical Abstract

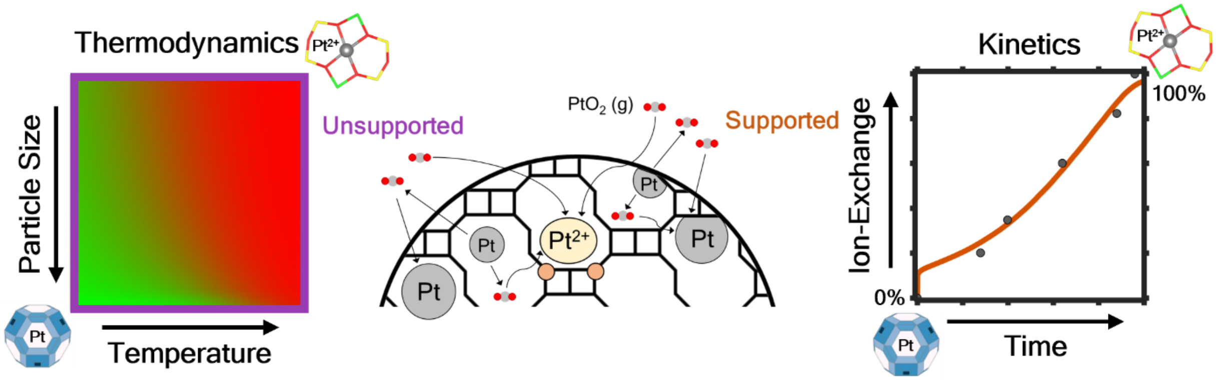

1. Introduction

The catalytic behavior of supported Pt catalysts is affected by particle sintering and redispersion [1–6], which are processes that dynamically restructure Pt sites and their ensembles in ways that may activate or deactivate specific active sites. The optimal active site structure depends on the catalyst application and may consist of a single or multiple metal atoms [3,6–8], and depending on the reaction environment these species can dynamically interconvert between single atoms and nanoparticles via particle redispersion and agglomeration processes [1,2,9,10]. Redispersion and sintering are also affected by the nature of the support [11–14], which further alters Pt site interconversion thermodynamics and kinetics. Therefore, an improved fundamental understanding of the thermodynamic and kinetic factors that influence redispersion and agglomeration processes for supported Pt particles would provide more precise guidance for identifying synthesis and regeneration conditions for Pt catalysts on different support materials. Here, we develop and demonstrate computational approaches for modeling the thermodynamics and kinetics of interconversion between cations and nanoparticles for Pt-containing aluminosilicate zeolites and contribute to the emergent topic of modeling catalyst stability and regeneration.

Zeolites have been widely investigated as potential supports to attenuate the sintering of metal nanoparticle catalysts by providing binding sites and void spaces that can stabilize small metal clusters and single atoms. For Pt supported on zeolites, the stabilization of single Pt atoms at anchoring sites [1,2,4,9,10,15] is facilitated by the altered electronic structure and coordination of the metal to siloxane or aluminosiloxane rings within the zeolite framework [1,16]. The three-dimensional, cage-like structure of zeolites confers additional sintering resistance due to high energy barriers (~1.12-2.57 eV) associated with metal atom diffusion through zeolite pores [4,16]. Nevertheless, under certain reaction conditions, Pt particles or the atoms that comprise them may mobilize, enabling interconversion between different Pt metal structures [1,2,4,9]. The thermodynamics and kinetics of particle restructuring depend on the zeolite composition and topology, environmental conditions, and particle size. Under high temperature oxidative conditions, particles may disintegrate into smaller particles or single atoms. Conversely, low temperature reducing conditions facilitate particle agglomeration and growth [1,2,4,9,10,17]. Such reversible transformations between different metal species induced by varying reaction conditions have been explored in several studies for Rh on ZSM-5 for methane oxidation to methanol [18], redispersion of SnO_2 clusters in β-zeolites during ketone oxidation [19], Pt cluster formation from isolated atoms in Y zeolite during ethane dehydrogenation [20], high-temperature (>750 K) oxidations on single-site Pt and Pt clusters in high silica CHA [2,9,21] and MFI [13,22], and hydrothermal treatments of Pd nanoparticles with air and steam in MFI, MWW, and CHA zeolites [23–26].

Here, we extend previous models for interconversion between cations and nanoparticles [26–32] to redispersion of Pt particles in zeolites by analyzing the influence of the initial Pt particle size distribution and environmental conditions on the interconversion between Pt particles and cations.

We used density functional theory (DFT) calculations to determine the most stable Pt^{2+} cation structures and use free energy approximations for supported and unsupported nanoparticles [33–35] to estimate the size-dependent energies of encapsulated Pt particles in CHA zeolites. We combine these cation and particle energies at different particle sizes and environmental conditions (P_{O2}, P_{H2O}, P_{H2}, T) to develop thermodynamic phase diagrams for Pt speciation within the zeolite. The phase diagrams demonstrate that at low temperatures, at large initial particle size distributions, and under hydrating and reducing conditions, conversion from Pt particles to cations is negligible. Conversely, high temperature and oxidizing conditions favor cation formation, consistent with experimental data reported at the same conditions. The thermodynamic models were then extended to BEA, TON, and MFI zeolites and validated with experimental literature reports. Ostwald ripening (OR) kinetic Monte Carlo (kMC) simulations show that the supported particle free energy model best describes experimentally observed interconversion kinetics for Pt-CHA, and model parameterization suggests van der Waals-induced stabilization of Pt particles.

2. Methods

2.1 DFT and AIMD Calculations

We used the Vienna ab initio simulation package (VASP, version 5.4.4) [36] to perform spin-polarized periodic, plane-wave calculations with an energy cutoff of 400 eV and projected augmented wave (PAW) method for core-valence interactions [37,38]. We used the 12 and 24 T-site 1Al and 2Al Pd-exchanged structures in SSZ-13 (CHA) from Mandal et al. [39], with the Pd atoms replaced by Pt atoms, and bulk Pt, α-PtO_2 (space group: p-3m1), and Pt_3O_4 (space group: Pm-3n) structures reported in the Materials Project database [40] as initial guesses and optimized the structures with the Perdew-Becke-Ernzerhof (PBE) functional [41], followed by the Heyd-

Scuseria-Erzenhof (HSE06) [36,41–46] functional. For the Pt and Pt-oxide bulk structures, we used the k-point mesh detailed in the Materials Project database [40] and for the zeolite structures, we used only the Γ point. We used self-consistent field (SCF) electronic energies and atomic forces convergence criteria of 10^{-8} eV and 0.01 eV/Å for calculations with the PBE functional and of 10^{-6} eV and 0.03 eV/Å for calculations with the HSE06 functional. We incorporated dispersion corrections for all calculations with the Becke-Johnson damping (D3(BJ)-vdw) method [42,43]. To further optimize the SSZ-13 structures beyond their local minima, we used spin-polarized ab initio molecular dynamics (AIMD) simulations. The 60 ps NVT simulations (Nose-Hoover thermostat), with 0.5 fs time-steps, began with the local energy minima optimized structure and were run at 298 K with the PBE functional and D3(BJ)-vdw corrections. We then optimized the five lowest energy structures from the AIMD simulation's trajectories with PBE, followed by HSE06, and used the resulting lowest energy structure of the five for our thermodynamic calculations. All optimized geometries are provided in the CONTCARS attachment in the Supporting Information.

2.2 Ab Initio Free Energy Calculations

We calculated the 0 K energies, relative to bulk Pt, for cation species with O_2 and H_2O-based ligands and bulk oxide species using Eqs 1 (*=1-2; x=0-8; y=0-5) and 2 (a=1,3; b=0,2,4), respectively. Likewise, we used Eqs 3 and 4 to calculate relative free energies. For a given species, ZPE represents the zero-point vibrational energies and S^{vib} represents the vibrational entropies, both of which are derived from the calculated species frequencies. Frequencies were calculated for gas-species (H_2O, O_2, H_2), bulk Pt metal and metal-oxides, and CHA cation and framework species. We assumed that the frequencies for cations in other zeolite frameworks (TON, BEA, MFI) are comparable to those in CHA and thus used the CHA frequencies to calculate the free energies of all zeolite frameworks. The term ΔS^{ST} (Eq 5) accounts for the translational and rotational entropy difference between bare and ligand-covered Pt in the zeolite framework. This value was calculated using the Sackur-Tetrode equation, assuming that adsorbates retain ~2/3 of their gas-phase translational entropy [47,48]. $M_{\mathrm{x,y}}$ in the Sackur-Tetrode equation is the mass of the ligand(s) bonded to Pt. $\Delta\mu_i$ (Eq 6) represents the difference in chemical potential between 0 K and the environmental conditions for gas species *i*, where P° is the standard state pressure (1 atm) [49,50]. Gas species chemical potentials were calculated using the NIST JANAF thermochemical tables [51].

$$\Delta E_{\mathrm{x,y}}^{\mathrm{form}} = E_{\mathrm{Z_*PtH_xO_y}} - E_{\mathrm{Pt_{bulk}}} - \frac{\mathrm{x}}{2}\left(E_{\mathrm{H_2O}} - \frac{1}{2}E_{\mathrm{O_2}}\right) - \frac{\mathrm{y}}{2}E_{\mathrm{O_2}} (1)$$

$$\Delta E_{\mathrm{Pt_aO_{b_{bulk}}}}^{\mathrm{form}} = \frac{E_{\mathrm{Pt_aO_{b_{bulk}}}}}{\mathrm{a}} - E_{\mathrm{Pt_{bulk}}} - \frac{\mathrm{b}}{\mathrm{a}}\left(\frac{E_{\mathrm{O_2}}}{2}\right) (2)$$

$$\Delta G_{\mathrm{x,y}}^{\mathrm{form}}\left(T, \Delta\mu_{\mathrm{O_2}}, \Delta\mu_{\mathrm{H_2O}}\right) = \Delta E_{\mathrm{x,y}}^{\mathrm{form}} + ZPE_{\mathrm{x,y}} - T\left(\Delta S_{\mathrm{x,y}}^{\mathrm{ST}}(T) + \Delta S_{\mathrm{x,y}}^{\mathrm{vib}}(T)\right) - \frac{\mathrm{x}}{2}\Big(\Delta\mu_{\mathrm{H_2O}} -$$

$$\frac{1}{2}\Delta\mu_{\mathrm{O_2}}\Big) - \frac{\mathrm{y}}{2}\Delta\mu_{\mathrm{O_2}} (3)$$

$$\Delta G_{\mathrm{Pt_aO_{b_{bulk}}}}^{\mathrm{form}}\left(T, \Delta\mu_{\mathrm{O_2}}\right) = \Delta E_{\mathrm{Pt_aO_{b_{bulk}}}}^{\mathrm{form}} + ZPE_{\mathrm{Pt_aO_{b_{bulk}}}} - T\left(\Delta S_{\mathrm{Pt_aO_{b_{bulk}}}}^{\mathrm{vib}}(T)\right) - \frac{\mathrm{b}}{2\mathrm{a}}\Delta\mu_{\mathrm{O_2}} (4)$$

$$\Delta S_{\mathrm{x,y}}^{\mathrm{ST}}(T) = \left(E_{\mathrm{Z_*PtH_xO_y}} - E_{\mathrm{Z_*Pt}}\right) \approx \frac{2}{3}\mathrm{k_B}\ln\left[\left(\frac{2\pi M_{\mathrm{x,y}}\mathrm{k_B}T}{\mathrm{h}^2}\right)^{3/2}\left(\frac{\mathrm{k_B}T}{\mathrm{P}^{\circ}}\right)\frac{\mathrm{e}^{5/2}}{\mathrm{N_A}}\right] (5)$$

$$\Delta\mu(P, T) = \mathrm{R}T\ln\left(\frac{P}{\mathrm{P}^{\circ}}\right) (6)$$

Similar to Eqs 1 and 2, Eqs 7 and 8 represent the 0 K energy and free energy of Z_2Pt under reducing conditions (in H_2), respectively, relative to Pt bulk:

$$\Delta E_{\mathrm{z}}^{\mathrm{form}} = E_{\mathrm{Z_*PtH_z}} - E_{\mathrm{Pt_{bulk}}} - \frac{\mathrm{z}}{2}E_{\mathrm{H_2}} (7)$$

$$\Delta G_{\mathrm{z}}^{\mathrm{form}}\left(T, \Delta\mu_{\mathrm{H_2}}\right) = \Delta E_{\mathrm{z}}^{\mathrm{form}} - T\left(\Delta S_{\mathrm{z}}^{\mathrm{ST}}(T) + \Delta S_{\mathrm{Pt}}(T)\right) - \frac{\mathrm{z}}{2}\Delta\mu_{\mathrm{H_2}} (8)$$

To derive the equilibrium fraction of ion-exchanged Pt ($\frac{n_{\mathrm{Pt}}}{N_{\mathrm{Pt}}}$) at a given pressure, temperature, and initial particle size, we minimized the free energy of the cation-particle system (ΔG_{sys}) with respect to the amount of ion-exchanged Pt (n_{Pt}). Eqs 9-11 gives the free energy of the system assuming the ion exchange enthalpy is coverage-independent:

$$\Delta G_{sys.}(P,T,d) = n_{\mathrm{Pt}}\left(\Delta \bar{G}^{\mathrm{form}}_{\mathrm{x,y}} - \Delta \bar{G}^{\mathrm{form}}_{\mathrm{particle}}\right) - T\Delta S_{config.} \qquad (9)$$

$$\Delta \bar{G}^{\mathrm{form}}_{\mathrm{particle}}(P,T,d) = \frac{\sum_{\mathrm{i=Pt,\alpha-PtO2,Pt3O4}}\left(\Delta G_{\mathrm{i}}\exp\left(\frac{-\Delta G_{\mathrm{i}}}{\mathrm{RT}}\right)\right)}{\sum_{\mathrm{i=Pt,\alpha-PtO2,Pt3O4}}\left(\exp\left(\frac{-\Delta G_{\mathrm{i}}}{RT}\right)\right)} \; (10)$$

$$\Delta \bar{G}^{\mathrm{form}}_{\mathrm{x,y}}(P,T,d) = \frac{\sum_{\mathrm{i=Z2Pt\,,Z2Pt(H2O)2}}\left(\Delta G_{\mathrm{i}}\exp\left(\frac{-\Delta G_{\mathrm{i}}}{RT}\right)\right)}{\sum_{\mathrm{i=Z2Pt\,,Z2Pt(H2O)2}}\left(\exp\left(\frac{-\Delta G_{\mathrm{i}}}{RT}\right)\right)} \; (11)$$

Here, $\Delta \bar{G}^{\mathrm{form}}_{\mathrm{particle}}(P,T,d)$ is the Boltzmann averaged free energy (relative to bulk Pt) of each particle species (i=Pt, α-PtO_2, and Pt_3O_4) computed using Eq.18 or Eq.19. Similarly, $\Delta \bar{G}^{\mathrm{form}}_{\mathrm{x,y}}(P,T,d)$ is the Boltzmann averaged free energy (relative to bulk Pt) of the cationic species (i= Z_2Pt and $Z_2Pt(H_2O)_2$) with their respective x, y values as denoted in Eq.1. The configurational entropy of cationic species in the zeolite lattice ($\Delta S_{\mathrm{config.}}$) is excluded when calculating $\Delta \bar{G}^{\mathrm{form}}_{\mathrm{x,y}}(P,T,d)$ and treated separately in Eq 9. The number of configurations for ion-exchanged Pt is computed as a function of $\varphi = \frac{N_{\mathrm{Pt}}}{N_{\mathrm{2Al}}} = \frac{\text{Total number of Pt atoms in the systyem}}{\text{Total number of exchange sites}}$ (Eq. 14, S1, and S2) and the expression was then simplified using Stirling's approximation (Eq. S3) to obtain $\Delta S_{\mathrm{config.}}$. Minimizing ΔG_{sys} with respect to the amount of ion-exchanged Pt (n_{Pt}) gives the fraction of cationic species at equilibrium (Eq 12):

$$X_{\mathrm{cation,tot}}(P,T,d) = \frac{n_{\mathrm{Pt}}}{N_{\mathrm{Pt}}} = \frac{\sqrt{(\varphi+1)^2 f^2 + 4\varphi\,(1-f)f} - (\varphi+1)f}{2(1-f)\varphi} \; (12)$$

where the Boltzmann factor partitioning free energies of particles and cationic species in the system is denoted as $f(\mathrm{P,T,d})$

$$f(P,T,d) = \exp(\frac{-(\Delta\bar{G}_{\mathrm{x,y}}^{\mathrm{form}} - \Delta\bar{G}_{\mathrm{particle}}^{\mathrm{form}})}{\mathrm{R}T}) \quad (13)$$

and φ is defined as the ratio between total number of Pt atoms in the system to the total number of 2Al pairs available for ion exchange:

$$\varphi = \frac{N_{\mathrm{Pt}}/N_{\mathrm{Al}}}{N_{\mathrm{2Al}}/N_{\mathrm{Al}}} = \frac{N_{\mathrm{Pt}}}{N_{\mathrm{2Al}}} = \frac{\text{Total number of Pt atoms in the systyem}}{\text{Total number of exchange sites}} \quad (14)$$

To calculate the fraction of Pt for each different species, we used the Boltzmann factors associated with each species and mass conservation (Eqs 15-16):

$$X_{\mathrm{cation,i}}(P,T,d) = \frac{X_{\mathrm{cation,tot}} \exp(\frac{-\Delta G_{\mathrm{i}}}{\mathrm{R}T})}{\sum_{\mathrm{i=Z2Pt,Z2Pt(H2O)2}}(\exp(\frac{-\Delta G_{\mathrm{i}}}{\mathrm{R}T}))} \quad (15)$$

$$X_{\mathrm{particle,i}}(P,T,d) = \frac{(1 - X_{\mathrm{cation,tot}}) \exp(\frac{-\Delta G_{\mathrm{i}}}{\mathrm{R}T})}{\sum_{\mathrm{i=Pt,\alpha-PtO2,Pt3O4}}(\exp(\frac{-\Delta G_{\mathrm{i}}}{\mathrm{R}T}))} \quad (16)$$

2.3 Pt Particle Size-Dependent Models

For calculating Pt metal and Pt-oxide surface energies, we used the Python Materials Genomics (*Pymatgen*) package. We used the built-in *Slabgenerator* function [52–54] to construct symmetric slabs, with Miller indices of ≤3 (Table S2.2) for Pt, for Pt, α-PtO_2, and Pt_3O_4 from their respective, optimized bulk structure. The slabs were 10 Å in thickness and had a 12 Å vacuum space to avoid periodic interactions between surfaces in the z-direction. To calculate the energies of these structures, we scaled the k-point mesh in the x and y directions by the ratio of the bulk to slab dimensions in the x and y directions, respectively. The k-point mesh in the z direction was set to one. We optimized the Pt and Pt_3O_4 slab structures with the PBE-D3(BJ)-vdw functional, using the same convergence criteria used with the bulk structures, to minimize computational expense. We chose to compute relative surface energies for α-PtO_2 with the HSE06-D3(BJ)-vdw functional to ensure that the calculated surface energies were not negative (which is an issue for α-PtO_2

specifically) and remained physically reasonable over all conditions. We calculated the surface energy (γ_{slab}) of each facet with Eq 17 [55]:

$$\gamma_{\mathrm{slab}}(P_{O_2},T) = \frac{E_{\mathrm{slab}} - n_{\mathrm{bulk}}E_{\mathrm{bulk}} - n_{\mathrm{O}}\mu_{\mathrm{O}}(P_{O_2},T)}{2A} \quad (17)$$

where n_{bulk} represents the number of units of the bulk structure and n_{O} represents the number of O atoms, in excess or deficit of the bulk units, in the slab, μ_{O} is the chemical potential of O, A is the surface area of one face of the slab, E_{slab} is the total, DFT-calculated energy of the slab, and E_{bulk} is the energy of one unit of the relevant bulk structure. We calculated the equilibrium average surface energies (γ_{avg}) and shape factors (η) of the Pt metal and oxides, ignoring particle size-dependence, by using *Pymatgen*'s *Wulffshape* function to generate their respective Wulff constructions [56]. With the input of γ_{slab} for each species' facets, the function outputs the average surface energies and shape factors at a range of μ_{O} values. At the oxidizing conditions we explored, μ_{O} ranges from -9.3 to -4.1 eV and we neglected the influence of hydroxyl groups on nanoparticles while evaluating the surface energies. Similarly, under conditions of H_2 exposure, we neglected the influence of adsorbed hydrogen species and only considered Pt nanoparticles with no adsorbates and Z_2Pt to be present in the system. Although H* and OH* coverages can decrease particle surface energies by about 0-25 meV/Å^2 [57] under the conditions we explored ($P_{H2O} < 10$ kPa, $550\ K<T<1350\ K$), our sensitivity analysis with $\gamma_{\mathrm{avg,Pt}} \pm 35$ meV/Å^2 (Figure S2.5-2.6) implies these changes have a minimal impact on the equilibrium ion-exchange predictions (Fig. S2.6).

To calculate the effect of particle size-dependence on free energy, we examined thermodynamic predictions with both supported and unsupported free energy model corrections. The supported model (Eq 18), based on calorimetric measurements of metals on oxide supports and developed by Campbell et al., describes the free energy, relative to the bulk free energy of formation, for a supported hemispherical particle of diameter *d* [33,58,59]. Here, *d* is the effective diameter, such that the d of a metal oxide particle is equal to the diameter of a Pt metal particle comprised of an equivalent number of Pt atoms. In addition, $E_{\mathrm{adh.}}(P_{\mathrm{O_2}}, T)$ is the adhesion energy between a particle and support, and ρ is the volume per mole of metal or metal oxide. Eq 18 reduces to Eq 20 when $E_{\mathrm{adh.}}(P_{\mathrm{O_2}}, T)$ is approximated with the Young-Laplace equation (Eq. 19), where θ is the contact angle between the spherical cap-like particle on a flat support. In the absence of a known $E_{\mathrm{adh.}}$ for the Pt metal and oxide particles supported on the zeolite, we considered θ = 60°, 90°, and 120° to represent a range of adhesion strengths (Fig. S2.1). The lack of variance in thermodynamic predictions between the different contact angles allowed us to select θ = 90° for the remaining thermodynamic calculations.

$$\Delta G_{\mathrm{sup}}(d, P_{\mathrm{O_2}}, T) = (3\gamma_{\mathrm{avg}}(P_{\mathrm{O_2}}, T) - E_{\mathrm{adh.}}(P_{\mathrm{O_2}}, T))(1 + \frac{1.5\ \mathrm{nm}}{d})(\frac{2\rho}{d}) \quad (18)$$

$$E_{\mathrm{adh.}}(P_{\mathrm{O_2}}, T) = \gamma_{\mathrm{avg}}(P_{\mathrm{O_2}}, T)(1 + \cos(\theta)) \quad (19)$$

$$\Delta G_{\mathrm{sup}}(d, P_{\mathrm{O_2}}, T) = \gamma_{\mathrm{avg}}(P_{\mathrm{O_2}}, T)(2 - \cos\theta)(1 + \frac{1.5\ \mathrm{nm}}{d})(\frac{2\rho}{d}) \quad (20)$$

The unsupported model (Eq 21), based on work by Sun et al., describes the free energy, relative to the bulk free energy of formation, for an unsupported spherical particle, of effective diameter d, in a vacuum [34,35]. For this model, at $d > 2$ nm, the free energy is described by a Gibbs-Thomson-like equation. At $d < 2$ nm, we used the PBE-D3(BJ)-vdw functional to optimize and calculate the energies of Pt particle structures from Ignatov et al. [60] up to 260 Pt atoms (~2 nm). These energies were interpolated using a cubic spline to determine $\Delta G_{\mathrm{interp}}$, which provides free energy estimates for any particles with $d < 2$ nm. The piecewise nature of $\Delta G_{\mathrm{unsup}}$ corrects for the shape factor and average surface energy dependence on particle size at $d < 2$ nm (Fig. S2.2) [28].

$$\Delta G_{\mathrm{unsup}}(d, P_{\mathrm{O_2}}, T) = \begin{cases} \Delta G_{\mathrm{interp}}(d),\ d < 2\ \mathrm{nm} \\ \eta\gamma_{\mathrm{avg}}(P_{\mathrm{O_2}}, T)\left(\frac{2\rho}{d}\right),\ d > 2\ \mathrm{nm} \end{cases} \quad (21)$$

To generate thermodynamic predictions, we calculated the fraction of a given Pt species in the system with the size-corrected ΔG values. Table S2.3 lists the assumptions used in the construction of the thermodynamic models.

2.4 Modeling Gas-phase Mediated Kinetics for Pt Redispersion

To model the redispersion of Pt metal to ion-exchanged Pt^{2+}, we used the kinetic theory of gases and collision theory. The monomers are generated via a gas phase OR process (Eq 22), and the process is modeled via Eq 23.

$$\mathrm{Pt_k} + \mathrm{O_2} \leftrightarrow \mathrm{PtO_2(g)} + \mathrm{Pt_{k-1}} \qquad (22)$$

A monomer ejected from the surface of a Pt particle may either bind to another Pt particle or exchange as a Pt ion at a Z_2H_2 site. Therefore, we represent the competitive redispersion kinetics of the Pt-zeolite system by coupling Eqs 23 and 27. In Eq 24, K_{os} is the pre-exponential factor for OR, C_{k} is the concentration of particles (per nm^{-2}) comprised of k Pt atoms, and A_k is the exposed surface area of the same particle. The sticking coefficient (S) of monomers was assumed to be 1 when calculating K_{os} (Eq 22), and $m_{\mathrm{PtO_2(g)}}$ is the molecular mass of $\mathrm{PtO_2(g)}$.

$$\frac{\mathrm{d}C_k}{\mathrm{dt}} = \begin{cases} -K_{\mathrm{os}}C_kA_k(P_{\mathrm{b}} - P_k) + K_{\mathrm{os}}C_{k-1}A_{k-1}(P_{\mathrm{b}} - P_{k-1}), P_k < P_{\mathrm{b}} \\ 0,\ P_k = P_b \\ K_{\mathrm{os}}C_kA_k(P_{\mathrm{b}} - P_k) - K_{\mathrm{os}}C_{k+1}A_{k+1}(P_{\mathrm{b}} - P_{k+1}), P_k > P_{\mathrm{b}} \end{cases} \qquad (23)$$

$$K_{\mathrm{os}} = \frac{S}{\sqrt{2\pi m_{\mathrm{PtO_2(g)}}\mathrm{k_B}T}} \qquad (24)$$

Depending on how the equilibrium monomer pressure of a particle (P_{k}) compares to the background monomer ($\mathrm{PtO_2}$) pressure (P_{b}) of the particle ensemble, the given particle will grow ($P_{\mathrm{k}} < P_{\mathrm{b}}$) or shrink ($P_{\mathrm{k}} > P_{\mathrm{b}}$) [26,61,62]. Considering $\mathrm{PtO_2(g)}$ mass conservation, P_{b} is given by the weighted average (by total exposed area) of equilibrium particle pressures [61]:

$$P_{\mathrm{b}}=\frac{\sum_k A_k n_k P_k}{\sum_k A_k n_k} \quad (25)$$

where n_k is the number of Pt particles comprised of k atoms, and P_k is the pressure of PtO_2 (g) in equilibrium with a Pt particle comprised of k atoms at a given oxygen pressure. P_k is the product of oxygen partial pressure (P_{O_2}) and the equilibrium constant between PtO_2 (g) and the Pt particle (Eq 26), which depends on the formation energy of the PtO_2 (g) monomer ($\Delta G^{\mathrm{form}}_{\mathrm{monomer}}$), and the free energy of the particle.

$$P_k = P_{\mathrm{O}_2} \exp\left(\frac{-\Delta G^{\mathrm{form}}_{\mathrm{monomer}} + \Delta G(d, P_{\mathrm{O}_2}, T)}{\mathrm{k_B} T}\right) (26)$$

The collision frequency between gas monomers and atom-trapping (Z_2H_2) sites is given by,

$$\frac{\mathrm{d}\theta_{\mathrm{Z_2Pt}}}{\mathrm{dt}} = \frac{(1-\theta_{\mathrm{Z_2Pt}})P_{\mathrm{b}}S}{N_0\sqrt{2\pi m_{\mathrm{PtO_2}}\mathrm{k_B}T}} \qquad (27)$$

which describes the change in the fraction of occupied atom-trapping sites with time [26]. In Eq 27, θ_{Z2Pt} is the fraction of trapping sites occupied with Pt, S is the sticking coefficient, and N_0 is the density of trapping sites (per nm^{-2}). We evaluated N_0 by assuming spherical CHA crystallites with a diameter of 50 nm and Si/Al = 8.5, consistent with the data reported by Moliner et al. [2], a random Al distribution, and a framework density for CHA of 15.1 T atoms/ 1000 Å^3. The monomer formation free energy term ($\Delta G^{\mathrm{form}}_{\mathrm{monomer}}$) will be different for the supported or unsupported Pt nanoparticle free energy models (Eq. 18,21). A sample code for the simulations is provided as a Supporting Information attachment file.

To simulate redispersion kinetics under different conditions, we first generated three unsupported (assuming spherical particles) and five supported (assuming ~hemispherical particles) log-normally distributed (LND) particle size distributions (Tables S3.1 and S3.2) consistent with the initial Pt-Pt coordination number of 7.36 (Fig S3.1) observed experimentally by Moliner et al.

[2]. Subsequently, we solved the system of differential equations defined by Eqs 23 and 27 using kMC. As kMC is a stochastic method, we averaged 20 independent simulations to obtain predictions. Fig. S3.2 demonstrates that the kMC simulations converge by 20 iterations. Using the kMC simulations for particle's supported and unsupported free energy models, we explored two types of temperature behaviors that correspond to the specific experiments in [2]. The first temperature behavior was a temperature ramp from 293 K to 773 K, at a rate of 10 K min^{-1}. The second behavior was sequential isothermal treatments (373, 473, and then 773 K), each held for 120 minutes before stepping to the next temperature. From the simulations, we obtained the extent of ion exchange and particle size distributions as a function of time and calculated the average Pt-Pt coordination number. To calculate the coordination number from the number of atoms in the particle, we interpolated the number of Pt atoms in a particle and the Pt-Pt coordination number reported by de Graaf et al. [63]. We used the MATLAB tool GRABIT [64] to extract the initial particle size distribution, the extent of conversion over time, and Pt-Pt coordination numbers from Moliner et al. [2]. Finally, we compare those experimental observations with our simulation results. Table S3.11 lists assumptions considered in the construction of the kinetic model.

2.5 Details of Zeolite Structure Sampling

To sample possible CHA (36 T-site supercell), BEA (64 T-site supercell), and TON (48 T-site supercell) Pt zeolite structures, we generated initial Z_2Pt and Z_2H_2 structures based on the pure silica form of the zeolite supercells from the international zeolite association (IZA) database. We repeated IZA zeolite unit cells until each cell vector was greater than 10 Å to avoid self-interactions between atoms due to periodic effects. From these supercells, we generated all possible two Al configurations (Z_2) within 10 Å. To determine the symmetrically unique Z_2 configurations, we used a connectivity-based graph isomorphism test using Python NetworkX code [65], similar to prior work [66]. All configurations with Al-O-Al were removed because according to Löwenstein's Rule [67,68], Al-O-Al bond formation in zeolites is unlikely. The Pt and H atoms, for the Z_2Pt and Z_2H_2 structures, respectively, were placed inside the zeolite rings using vector Eqs 28 [69] and 29 [70]:

$$\mathbf{Al - Pt} \ = (\mathbf{Al - O1}) + (\mathbf{Al - O2}) \ (28)$$

$$\mathbf{H - O -} = 0.98\left(\frac{(\mathbf{O - T1}) - (\mathbf{O - T2})}{|(\mathbf{O - T1}) - (\mathbf{O - T2})|}\right) \ (29)$$

Here, O1 and O2 are bound to the same Al, and T1 and T2 are T-site atoms bound to the same O. These equations place Pt in the plane generated by Al-O1 and Al-O2, and H atoms on the plane generated by O-T1 and O-T2 [70], with an O-H distance of 0.98 Å. Once we placed the Pt and H atoms, we performed another graph isomorphism test to remove any similar structures. We optimized the remaining structures with the PBE-D3(BJ)-vdw functional, followed by the HSE06-D3(BJ)-vdw functional. Our calculations for CHA and TON showed that the low energy Z_2Pt and low energy Z_2Cu structures reported in previous studies [66] have analogous coordination to the zeolite framework. Therefore, for BEA, based on previously reported Z_2Cu structures [66], for BEA we only sampled eight candidate minimum energy Z_2Pt structures.

3. Results and discussion

3.1 Pt cation speciation in CHA zeolites

We identified the lowest energy Pt cation structure in CHA zeolites (Fig. 1a) by considering structures with either one Al ("Z") or two Al ("Z_2") T-sites with different Al pair configurations, and ligands. For the 1Al exchange site, all T-site positions for Al in CHA are crystallographically equivalent, therefore all ZPt sites are the same. For the two Al exchange sites, we computed the relative energies of Z_2Pt structures with different Al pair configurations (Fig. S1.1). The lowest energy Z_2Pt zeolite structure, similar to other ion-exchanged Pt-group metals like Cu [71], and Pd [39], contains a Pt^{2+} cation populating a six-membered ring (6MR) with two Al separated by two Si atoms (third nearest neighbor [3NN] configuration; Fig. 1b), similar to the lowest energy structures reported for Cu and Pd exchange in CHA zeolites [39,71].

We next calculated energies for different numbers of H- and O- ligands attached to the ionic Pt atoms in the Z_2Pt and ZPt structures (Fig. 2a, b). To determine the Pt species that are most thermodynamically stable at a given set of environmental conditions, we first calculated the 0 K energies for all the cationic Pt motifs considered ($Z_*PtH_xO_y$) using the HSE06 functional with D3(BJ)vdw dispersion correction, and then used thermodynamic correlations detailed in Section 2.2 to compute the Gibbs free energies (ΔG_{form}) of these structures relative to Z_2Pt as a function of T, P_{O2}, and P_{H2O}. A comparison of $\Delta G_{form}(T, P_{O2}, P_{H2O})$ for all $Z_*PtH_xO_y$ species shows that Z_2Pt, along with H_2O-solvated Z_2Pt ($Z_2Pt(H_2O)_{x=2,4}$), are the most stable conformers over a wide range of conditions (Fig. 1b, 2a, and S2.3). More specifically, the Z_2Pt and $Z_2Pt(H_2O)_2$ structures persist as the most stable Pt zeolites structure under all temperatures and environmental conditions of interest for interconversion between cations and nanoparticles [61] ($T > 550$ K, $P_{H2O}/P_{O2} < 0.5$ at $P_{O2} = 20$ kPa).

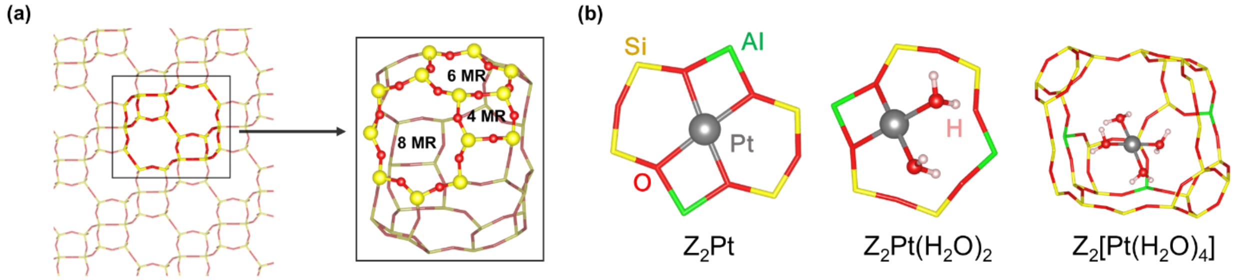

Figure 1. (a) Framework of CHA with cutout of cage, comprised of four, six, and eight member rings, from a periodic supercell and (b) the HSE06-D3(BJ)vdw-optimized structures of the most stable Pt/CHA species.

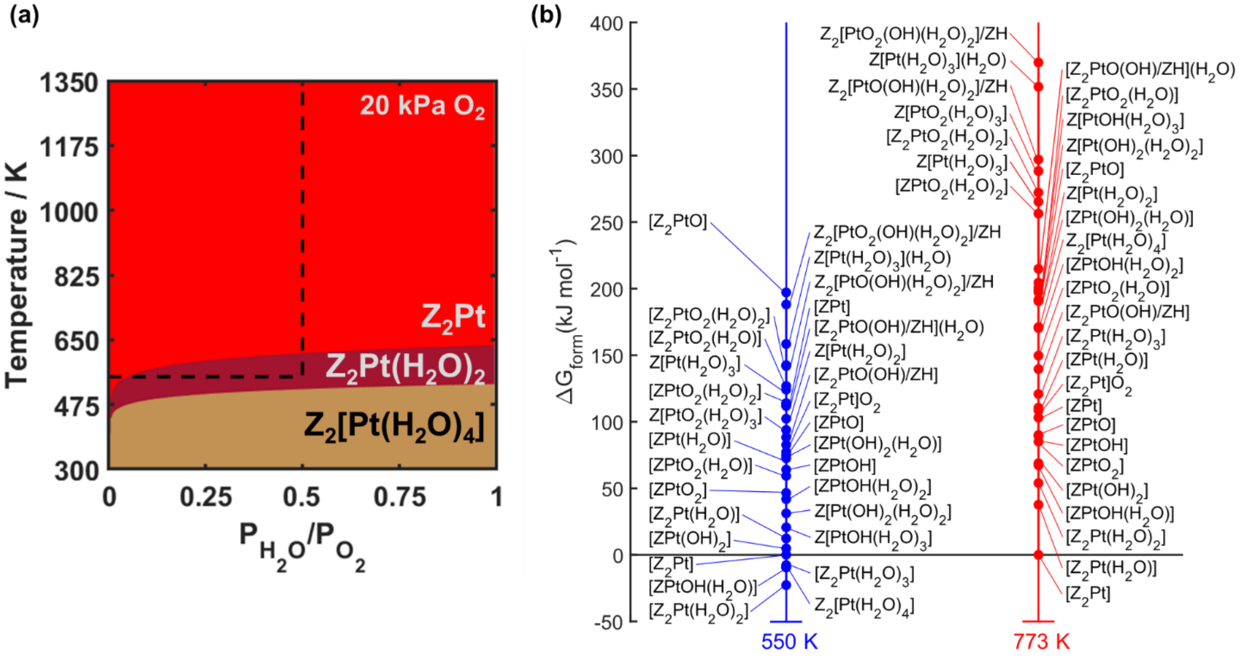

Figure 2. (a) Phase diagram of the most stable Pt/CHA species at different pressures and temperatures. The dotted line represents the boundary of the conditions of interest for interconversion. (b) Free energies of $Z_{(1-2)}PtH_xO_y$ species at 10 kPa H_2O and 20 kPa O_2 for 550 K (blue) and 773 K (red). The Z enclosed in brackets, for example, as in $[Z_2Pt(H_2O)_2]$ represents anionic $[AlO_4]^-$ that are chemically bonded to Pt (Pt-O$_{framework}$ ~2.1 Å). In contrast, Z outside of

the brackets e.g. $Z_2[Pt(H_2O)_4]$ represents anionic $[AlO_4]^-$ that only interact with Pt via Van der Waals and electrostatic interactions ($Pt\text{-}O_{framework} > 3$ Å) .

3.2 Thermodynamics of Interconversion between Pt particles and Pt Cations

Under oxidizing conditions, our computational model consists of competing reactions that convert Pt metal into oxides (α-PtO_2, Pt_3O_4) (Eqs. 30 and 31, respectively) and ion-exchange reactions that convert metal and oxide particles to Z_2Pt cations (Eqs.32-34). We also analyzed the conversion of metal particles to cations under reducing conditions (Eq. 35), considering only Pt metal and adsorbate free Z_2Pt:

$$\mathrm{Pt_{bulk}} + \mathrm{O_2} \leftrightarrow \alpha\text{-}\mathrm{PtO_2} \qquad (30)$$

$$\mathrm{Pt_{bulk}} + \tfrac{4}{3}\mathrm{O_2} \leftrightarrow \tfrac{1}{3}\mathrm{Pt_3O_4} \qquad (31)$$

$$\mathrm{Pt_{bulk}} + \mathrm{Z_2H_2} + \tfrac{1}{2}\mathrm{O_2} \leftrightarrow \mathrm{Z_2Pt} + \mathrm{H_2O} \qquad (32)$$

$$\alpha\text{-}\mathrm{PtO_{2_{bulk}}} + \mathrm{Z_2H_2} \leftrightarrow \mathrm{Z_2Pt} + \mathrm{H_2O} + \tfrac{1}{2}\mathrm{O_2} \qquad (33)$$

$$\tfrac{1}{3}\mathrm{Pt_3O_{4_{bulk}}} + \mathrm{Z_2H_2} \leftrightarrow \mathrm{Z_2Pt} + \mathrm{H_2O} + \tfrac{1}{6}\mathrm{O_2} \qquad (34)$$

$$\mathrm{Pt_{bulk}} + \mathrm{Z_2H_2} \leftrightarrow \mathrm{Z_2Pt} + \mathrm{H_2} \quad (35)$$

We next computed the relative stability of the species in Eqs 30-35 (Section 2.2) by evaluating ΔG_{form} at the conditions of interest (550 K and 773 K, maximum $P_{H2O}/P_{O2} = 0.5$, $P_{H2} = 4$ kPa), relative to Pt_{bulk} using HSE06-D3(BJ)vdw computed energies. The computed formation energies for the Pt-oxide species (Table S2.1, Fig. S2.4), derived from Eqs. 30 and 31, are consistent with experimental and computational values reported in the literature [72–75].

The energies of Pt and Pt-oxides are sensitive to nanoparticle size. We estimated the size-dependent energy of Pt metal and Pt-oxide nanoparticles using two different models: supported and unsupported particles. These models bookend two extremes for calculating particle free energies. The supported model (ΔG_{sup}; Eq 18), which was developed by Hemmingson and Campbell, is consistent with calorimetry measurements of oxide-supported nanoparticles [33] and describes metal particles adhered to a support (the zeolite in this instance) by stabilizing nanoparticle energies relative to cations through the contribution of the adhesion energy. We previously used this model to estimate the free energy of Pd nanoparticles supported on the external surface of zeolite crystallites [26]. This adhesion energy is absent in the unsupported model (ΔG_{unsup}; Eq 21), which was developed by Sun et al. [34,35] and considers the metal particles to be in vacuum and is similar to the Gibbs-Thomson equation. In Pt-zeolites, Pt particles may be located on the external surface of the zeolite crystallites or encapsulated within the zeolite pores [76], which contain framework oxygen atoms that provide multiple weak points of contact to stabilize particles via van der Waals forces instead of requiring direct adhesion to the framework. Here, we considered both models and compared them to experimental studies to ascertain the model that best describes these systems and determine how encapsulation modulates nanoparticle energies.

Fig. 3 reports the resulting phase diagrams that show the equilibrium fraction of Pt atoms that form Pt metal particles, Pt-oxide particles, and Pt cations, represented by green, blue, and red, respectively, for a range of P_{O2}, P_{H2O}, P_{H2}, T, and particle size distributions in CHA. Here, we incorporate CHA structural information ($N_{Pt}/N_{Al} = 0.006$, Si/Al = 8.5) [2] and calculate $N_{2Al}/N_{Al} = 0.15$, assuming a random Al distribution and that the equilibrium population of $Z_2Pt(H_2O)_x$ and Z_2Cu in CHA is the same [66,71]. Both the supported and unsupported free energy models demonstrate that under dry conditions (P_{H2O}/P_{O2} = 5e-4), Pt cations are the most thermodynamically stable species over nearly the entire range of temperatures and particle sizes (Fig. 3a). This trend largely persists at increasing water pressure (P_{H2O}/P_{O2} = 0.50, Fig. 3b). In contrast, upon exposure to H_2, which promotes the reduction of Pt-oxide particles and Pt cations to Pt metal [4,13,17], only small particles (< 5 nm) at extremely high temperatures (> 1100 K) favor conversion to cations (Fig. 3c). At 4 kPa H_2, both models predict complete conversion to Pt metal particles at all particle sizes for temperatures below 923 K. The observed predictions hold if the Pt surface energy decreases by up to 25 meV/Å^2 due to the presence of adsorbed H on nanoparticles (Figs. S2.5-2.6) [57]. This complete thermodynamic reversibility between Pt cations and metal particles (< 923 K) through exposure to O_2 and H_2 is consistent with experimental observations at these conditions [2,9].

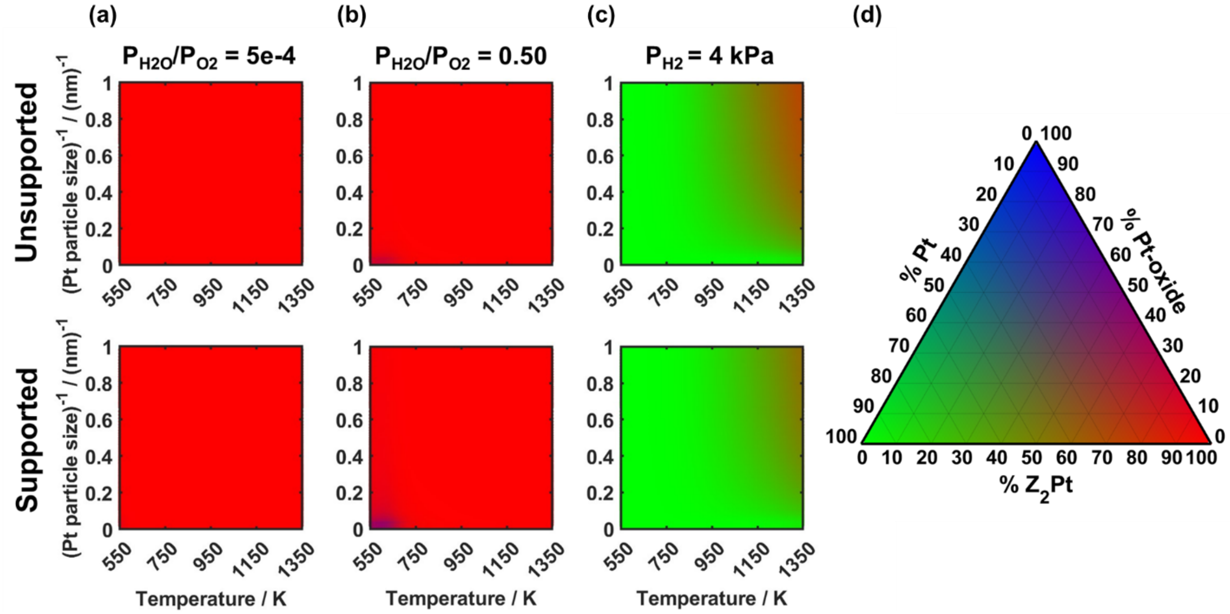

Figure 3. Pt particle size and temperature-dependent thermodynamic phase diagram for the conversion of Pt particles to Pt species in CHA (N_{Pt}/N_{Al} = 0.006, Si/Al = 8.5, N_{2Al}/N_{Al} = 0.15) at (a) P_{H2O} = 0.01 kPa and P_{O2} = 20 kPa, (b) P_{H2O} = 10 kPa and P_{O2} = 20 kPa, and (c) P_{H2} = 4 kPa. The top and bottoms rows represent predictions for the unsupported and supported free energy

models, respectively. (d) Color key for panels a-c that denotes red, green, and blue as Pt cations, Pt metal, and Pt-oxides, respectively.

Both of the free energy models predict results for Pt cation interconversion that are consistent with experimental reports [2], with only slight discrepancies between each other. Under wet conditions, at low temperatures (< 700 K) and large, initial average particle sizes (> 10 nm), both the unsupported and supported models predict a percentage (maximum of 32% and 53%, respectively, at 100 nm and ~610 K) of Pt-oxide particles, suggesting that certain low operating temperatures must be avoided to prevent particle formation. However, Pt-oxides are more pronounced in the supported model. Similarly, under exposure to H_2, smaller Pt metal particles persist at higher temperatures in the supported model. This difference is the consequence of the unsupported model treating large particles in vacuum as less stable relative to particles supported on the zeolite [33]. Both models predict 100% conversion to cations at most oxidizing conditions, including at an average initial particle size of 1.5 nm at 773 K, under dry conditions, which is consistent with experimental data from Moliner et al. at these conditions [2]. Model predictions that the addition of H_2 at 673 K favors full reversibility back to Pt particles are also in agreement with Moliner et al. [2], further suggesting that both of our models appear to accurately represent the thermodynamics of interconversion in CHA zeolites.

3.3 Extending CHA Thermodynamic Model to Other Zeolite Topologies

To demonstrate the generalizability of the two free-energy models to other zeolite topologies, we examined the predicted thermodynamics for the BEA, TON, and MFI frameworks. Each of these zeolites has a minimum energy Pt cation structure (see Section 2.5 for details of structure sampling) similar to that of CHA. The Pt cation structure of MFI is the same as Z_2Pt structure in

CHA, consistent with EXAFS data and DFT calculations from Felvey et. al. [22], with a Pt^{2+} cation in a 3NN 6MR 2Al configuration. The IR spectra of Pt ion-exchanged MFI and BEA also contain T-O-T stretching frequencies consistent with a Pt^{2+} cation in a 6MR 2Al site [22], and sampling different Al-pair configurations (Fig. S1.2a) indicates that the most stable cation structure is Pt^{2+} charge-compensating 3NN 6MR 2Al sites. The Z_2Pt 6MR 2Al site is the most stable cation location for CHA, BEA, MFI, and TON (Fig. S1.2b). Thus, we only consider adsorbate-free Z_2Pt 6MR 2Al sites for modeling the thermodynamics of the BEA, TON, and MFI zeolites, as adsorbates only impact predictions at the lowest temperatures.

Using the most stable cation structures for each of the zeolite frameworks and their associated ion-exchange energies (and $N_{2Al}/N_{Al} = 0.15$ and $N_{Pt}/N_{Al} = 0.006$ values consistent with CHA in Figure 3), we developed phase diagrams for the unsupported (Fig. 4) and supported (Fig. S2.9) Pt free-energy models. Analogous to the thermodynamic results for CHA, the models largely predict complete conversion to cations under dry and wet conditions for each of the zeolite topologies (Fig. 4, S2.9). Exposure to H_2 results in the formation of thermodynamically stable Pt particles at low temperatures. At higher temperatures and smaller particle sizes, each zeolite topology has different degrees of ion-exchange. The structural difference between zeolites likely impacts conversion to Pt cations through changes in ring strain and distortion in CHA (Fig. S2.10), BEA, MFI, and TON (Fig. 4c, f, i). Ring expansion due to ion-exchange, associated with more exothermic ion-exchange energies, results in more thermodynamically favorable Pt cation species [22,70,77–79]. Conversely, the more endothermic Pt exchange energy for CHA (Fig. S2.10) is associated with ring contraction. As a result, Pt^{2+} ions in TON (most exothermic exchange energy), BEA, and MFI will persist at lower temperatures in comparison to Pt^{2+} ions in CHA (least exothermic exchange energy). These results show that cation fractions, and therefore optimum environmental conditions for ion-exchange, are zeolite framework dependent.

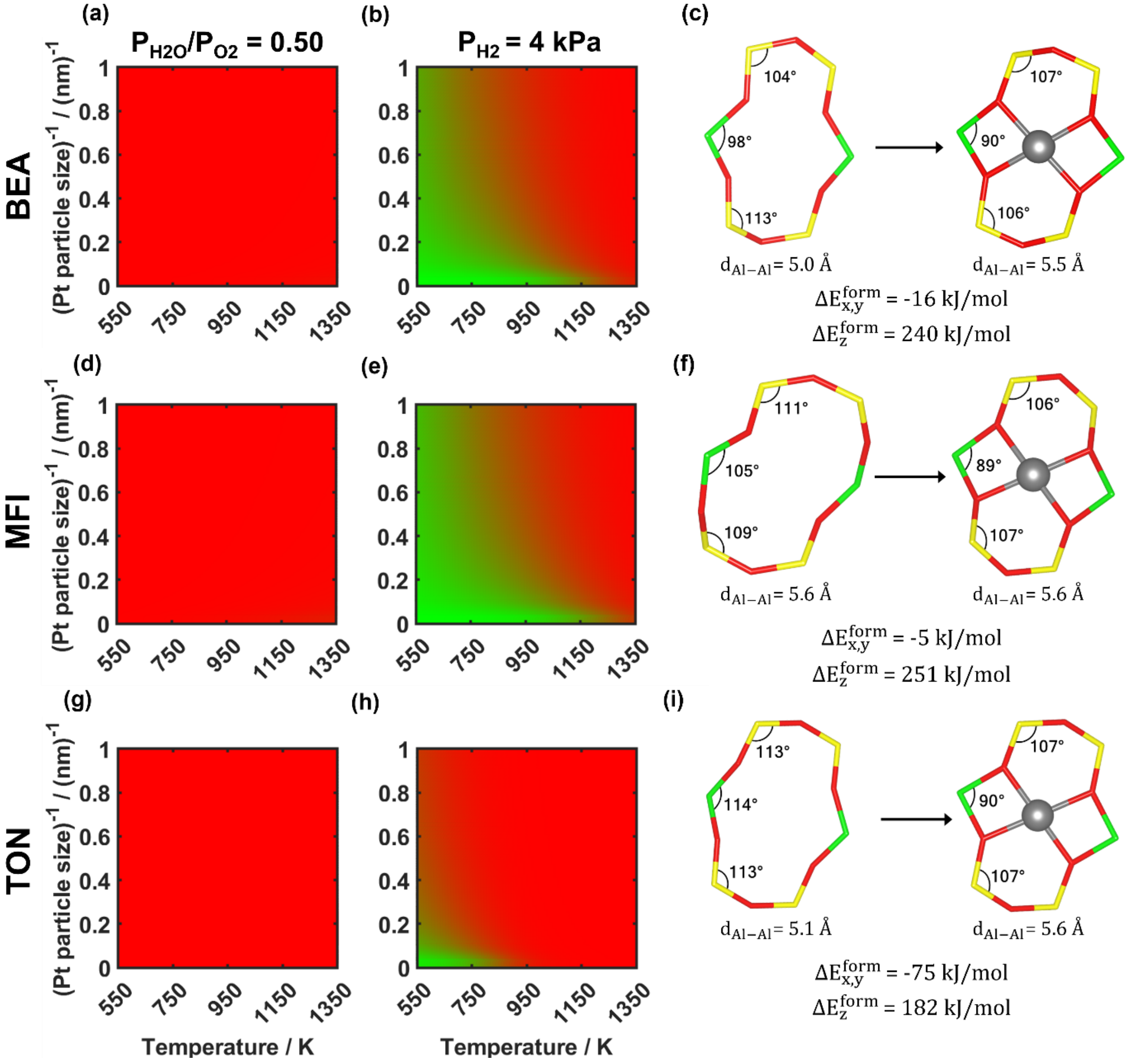

Figure 4. Pt particle size (using the unsupported particle free energy model, results for the supported model are shown in Fig. S2.9) and temperature-dependent thermodynamic phase diagrams for the conversion of Pt particles to Pt cations in (a, b) BEA, (d, e) MFI, and (g, h) TON. The diagrams (a, d, g) are calculated at P_{H2O} = 10 kPa and P_{O2} = 20 kPa, and (b, e, h) P_{H2} = 4 kPa. Zeolite structures show the 6 MR ring distortions from the Z_2H_2 frameworks (H atoms hidden for clarity) to ion-exchanged structures for (c) BEA, (f) MFI, and (i) TON. The exchange energies of

Pt atoms in each zeolite framework under exposure to O_2 and H_2O ($\Delta E_{\mathrm{x,y}}^{\mathrm{form}}$) and H_2 ($\Delta E_{\mathrm{z}}^{\mathrm{form}}$) are listed under the respective framework's structure.

These thermodynamic predictions for each zeolite, adapted for compositions reported for experimentally synthesized materials [22] (Fig. S2.11 and S2.12), are consistent with a number of experimental observations. Pt particles in MFI have been reported to undergo complete particle redispersion at 20% O_2 and 923 K, and subsequent exposure to 10% H_2 at 773 K results in Pt particle formation [22]. Both of these observations for MFI are consistent with the supported particle and unsupported particle model predictions over the range of modeled particle sizes. Across the range of modeled particle sizes, the thermodynamic predictions for BEA at 20% O_2 and 873 K also agree with experimental results that demonstrate the majority of Pt clusters in BEA redisperse to Z_2Pt after exposure to these conditions [22]. The overall thermodynamic consistency of both the unsupported and supported free-energy models across the three different zeolite frameworks indicates that while both models are useful for estimating the conditions where interconversion is thermodynamically favorable, thermodynamic considerations alone are incapable of discerning the more accurate free energy model for encapsulated Pt nanoparticle energies.

3.4 Kinetics of Interconversion of Pt particles to Ion-exchanged Pt Cations

The thermodynamic predictions for both supported and unsupported free energy models are consistent with reported experimental data [2,22]; therefore, our next aim is to discern the model that best describes the redispersion kinetics of encapsulated Pt nanoparticles to Pt cations. To describe the kinetics of Pt redispersion, our kinetic model assumes an Ostwald ripening (OR) mechanism (Eqs. 23, 27) to generate gas phase monomers that exchange between nanoparticles (analogous to the model developed by Plessow et al. [61]), coupled with reaction of monomers at Z_2H_2 ion-exchange sites in the zeolite (Scheme 1) [26]. In OR, particles disintegrate to generate mobile monomers (Eq 22), which under the conditions considered here are mobile, neutral, gas-phase PtO_2 (g) [80]. The gaseous monomers can traverse the zeolite and migrate to either other Pt particles, facilitating particle growth, or monomers may travel to and exchange at atom-trapping sites, which are the 2Al sites that exchange Pt to form Z_2Pt cations at the conditions of interest (negligible P_{H2O}, 20 kPa O_2). At these conditions, we assume that ion exchange is an irreversible process because equilibrium is heavily shifted towards cations at all temperatures, which is consistent with our thermodynamic predictions in Fig. 3a. To model the redispersion process, we simulated a two-step mechanism where the Pt metal particles eject monomers that compete to form either larger Pt metal particles or ion-exchanged Pt^{2+} (Scheme 1).

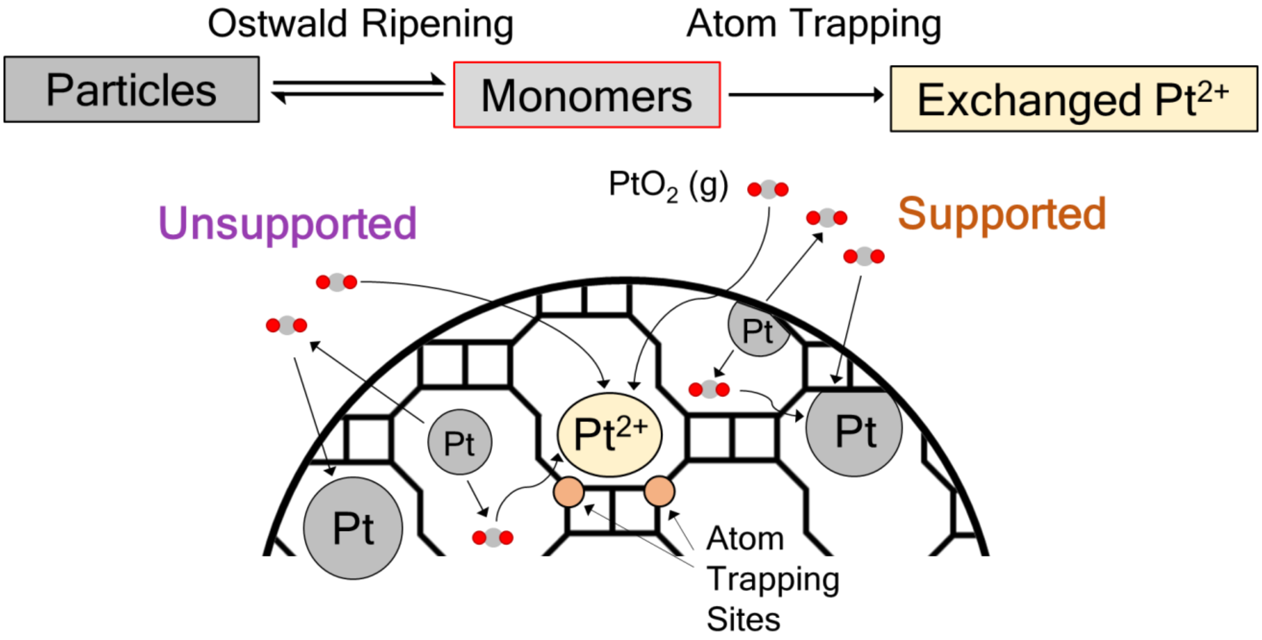

Scheme 1. Proposed scheme for unsupported and supported Pt particle redispersion and sintering, facilitated via gas-phase mediated Ostwald ripening with atom trapping sites.

To model time-dependent ion-exchange at different temperatures, we simulated the Pt particle-zeolite system (Scheme 1) using kMC with constrained parameters (Table 1). The parameters included the monomer formation energy ($\Delta G_{\mathrm{monomer}}^{\mathrm{form}}$) and nanoparticle surface energy ($\gamma_{\mathrm{avg,Pt}}$) for the unsupported particle model and the entire ($3\gamma_{\mathrm{avg,Pt}} - E_{\mathrm{adh}}$) term in the supported particle model. The average particle size ($\overline{\mathrm{x}}$) and the standard deviation ($\mathrm{s}_{\overline{\mathrm{x}}}$) of LND (consistent with TEM) particle size distributions were constrained (Fig S3.1) to satisfy the initial Pt-Pt coordination number of 7.36 ± 1.4 reported by Moliner et al. [2]. In the absence of energy estimates of $\gamma_{\mathrm{avg,Pt}}$ and $\Delta G_{\mathrm{monomer}}^{\mathrm{form}}$ for zeolite-encapsulated particles, size-dependent sticking coefficient estimates [61], and precise initial particle size distribution data, we searched for parameter sets ($\gamma_{\mathrm{avg,Pt}}$ or ($3\gamma_{\mathrm{avg,Pt}} - E_{\mathrm{adh}}$), $\Delta G_{\mathrm{monomer}}^{\mathrm{form}}$, $\overline{\mathrm{x}}$, and $\mathrm{s}_{\overline{\mathrm{x}}}$) starting with initial guesses consistent with surface energies for Pt nanoparticles in the absence of the zeolite framework: $\gamma_{\mathrm{avg,Pt}}$ = 96 meV/Å^2 (DFT-computed), E_{adh} = $\gamma_{\mathrm{avg,Pt}}$ [81] and $\Delta G_{\mathrm{monomer}}^{\mathrm{form}}$=1.69 eV [61]. The parameter ranges explored in the kinetics simulations resulted in negligible variations (Fig. S2.5-2.8) of thermodynamic predictions with both free energy models (Eq.18 and 21). First, we fit the kinetic model parameters by minimizing the sum of squared errors between the predicted and experimentally reported extent of atoms in Pt particles converted to Z_2Pt in Pt-CHA (grey points in Fig. 5a) during a linear temperature ramp from 293 to 773 K at 10 K min^{-1} in 20 kPa O_2 [2]. Next, we validated these regressed kinetic model parameter sets by comparing the simulated average Pt-Pt coordination numbers under sequential isothermal holds at 373, 473, and 773 K to the Pt-Pt coordination numbers from EXAFS reported in the same study [2] (Fig. 5b).

Table 1. Parameters used for gas-mediated ion-exchange mechanism

Parameter	Value
^1S	1

^2N_o	$1.98\text{x}10^8$ nm^{-2}
$^2P_{O2}$	20 kPa
$^3\gamma_{avg,Pt}$: for unsupported	40 – 105 meV/Å^2
$^3(3\gamma_{avg,Pt} - E_{adh.})$: for supported	110 – 210 meV/Å^2
$^3\Delta G^{form}_{monomer}$	1.30 – 1.85 eV
$^3\bar{x}$	0.5 – 1.5 nm
$^3s_{\bar{x}}$	0.18 – 0.48 nm

[1] Parameter value from Plessow et al. [61]

[2] Parameter value from Moliner et al. [2]

[3] Ranges of considered values for parameters

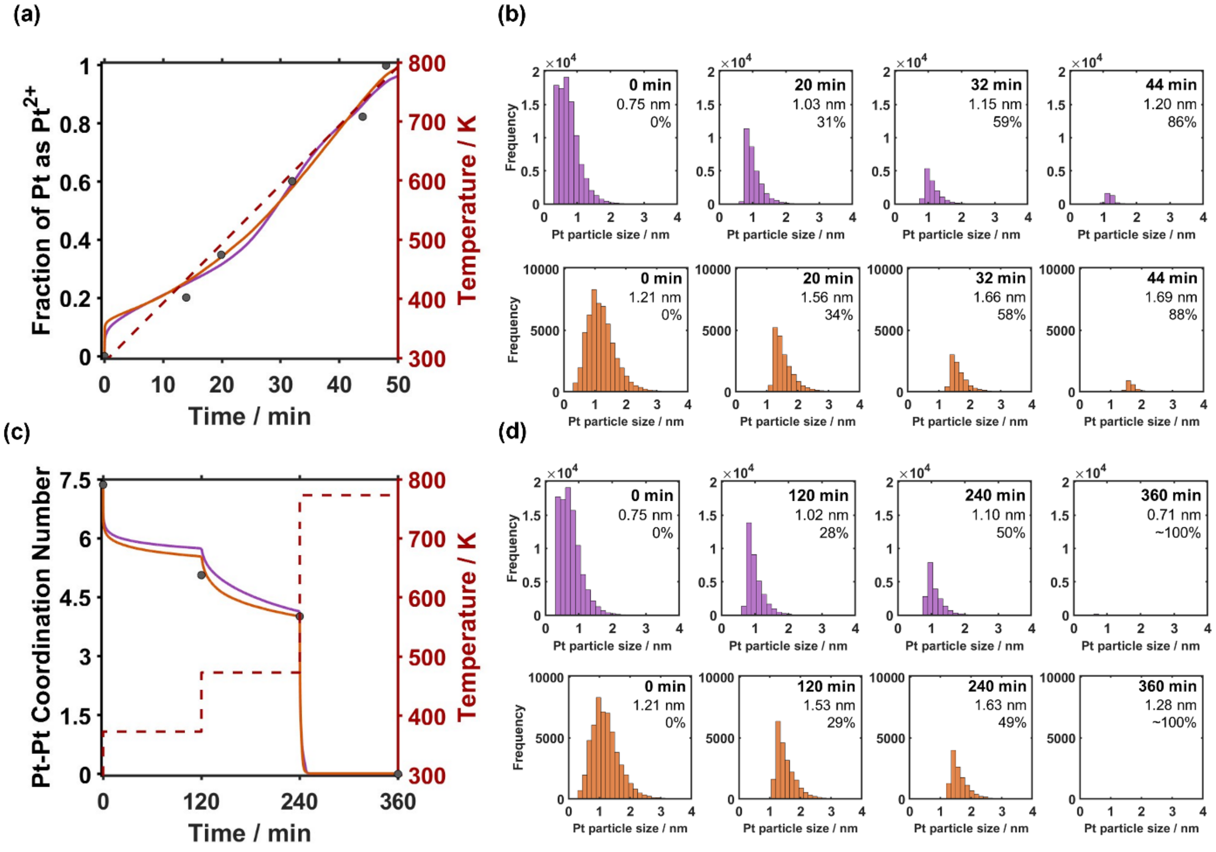

Figure 5. Kinetic model predictions (using kMC) for the (a) extent of ion-exchange with the temperature ramp and (b) Pt-Pt coordination numbers for the isothermal hold simulations. Purple ($\bar{x}$=0.75 nm) and orange ($\bar{x}$=1.25 nm) traces are the best-fit unsupported and supported free energy models, respectively. The grey points are experimental data from Moliner et al. [2].

Fig. 5a reports the best fit parameters for the fraction of Pt converted to Z_2Pt over time (grey points are experimental data). The kinetic model predictions for different particle size distributions (Table S3.1 and S3.2) were explored using a grid search of $\gamma_{\mathrm{avg,Pt}}$ (or $3\gamma_{\mathrm{avg,Pt}} - E_{\mathrm{adh.}}$ in the supported particle model) and $\Delta G_{\mathrm{monomer}}^{\mathrm{form}}$ (Tables S3.3-10) during parameter fitting, and are shown in Fig. S3.6 and S3.7. The surface energy, $\gamma_{\mathrm{avg,Pt}}$,, and the monomer formation free energy, $\Delta G_{\mathrm{monomer}}^{\mathrm{form}}$, primarily influence the initial rate of interconversion. For example, either a higher $\gamma_{\mathrm{avg,Pt}}$, or a lower $\Delta G_{\mathrm{monomer}}^{\mathrm{form}}$, result in higher rates of $PtO_{2(g)}$ monomer formation, leading to faster initial ion exchange (Fig. S3.3). The initial particle size distributions, each consistent with the experimental average Pt-Pt coordination number [2], control the slope of the interconversion curve (Fig. S3.4 and S3.5).

With the best-fit parameters, both the supported and unsupported models produce comparable accuracy (Table S3.3-3.10) for kinetic predictions (Fig. 5a) and validations (Fig. 5c). The distributions with $\bar{x}$=0.5 and 0.75 nm for the unsupported particle free energy model and $\bar{x}$ = 0.75, 1.25 nm for the supported particle free energy model predict Pt redispersion during the temperature ramp within a typical error for time-resolved XANES fitting (± 10% each datapoint) [82]. For each of these particle size distributions (PSD), we validated regressed parameter sets (Fig. S3.8 and S3.9) and found that $\bar{x}$=0.75 nm ($\gamma_{\mathrm{avg,Pt}}$ = 75 meV/Å^2, $\Delta G_{\mathrm{monomer}}^{\mathrm{form}}$=1.65 eV) and $\bar{x}$=1.25 nm ($3\gamma_{\mathrm{avg,Pt}} - E_{\mathrm{adh}}$ = 160 meV/Å^2, $\Delta G_{\mathrm{monomer}}^{\mathrm{form}}$=1.69 eV) best predict the average Pt-Pt coordination numbers (Fig. 5c) for the unsupported and supported models, respectively. However, the initial PSD of the best supported particle model is consistent with the reported TEM particle size distribution (and not just the avg. particle size estimated from EXAFS) [2] (Fig. S3.10d), while the unsupported model deviates significantly from this distribution (Fig. S3.10g). Therefore, we conclude that the supported particle model with the fit parameters above provides the best consistency with experimental data.

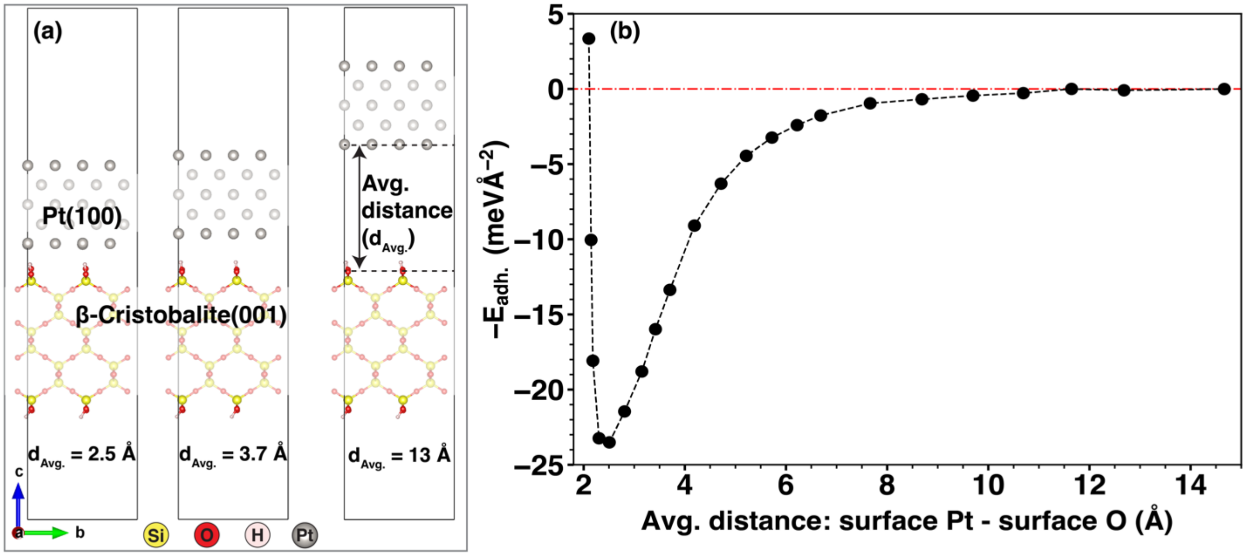

Figure 6. (a) Separated Pt(100) and hydroxylated silica slab, and (b) the change in adhesion energy (E_{adh}) between Pt on silica vs the average distance between surface Pt atoms and surface O atoms (on the silica slab). Non-surface atoms that were constrained in DFT optimizations are depicted with low opacity in (a).

In the best (supported particle) model, the regressed $\Delta G^{\mathrm{form}}_{\mathrm{monomer}}$ is equivalent to that for Pt nanoparticles on other supports [61,62], suggesting that the energy cost to eject a gas monomer from a Pt nanoparticle is not sensitive to zeolite encapsulation of the particle. To decouple the energy contributions of the regressed ($3\gamma_{\mathrm{avg,Pt}} - E_{\mathrm{adh}}$) value, we computed the distance-dependent interaction energy between a silica slab (as an approximate model for a high silica zeolite) and a Pt surface (Fig. 6a). The hydroxylated silica β-cristobalite (001) slab represents the internal or external zeolite surface, and the Pt(100) surface was used to represent Pt particles due to a minimal lattice mismatch with the silica slab. This is a rough approximation that does not account for several other factors that could influence the effective adhesion energy between Pt and the zeolite, such as the exact surface structure of the particle and temperature and water pressure dependent degree of hydroxylation of the silica slab [83, 84]. Hydroxylation makes the adhesion energy of Pt to silica more endothermic [83], and more hydroxylation is expected at lower temperatures [85, 86]. Fig. 6b shows that the attraction between Pt and the silica surface results in an adhesion energy of 24 meV/Å^2 at an ideal Pt-silica slab distance (2.5 Å). Using this computed E_{adh} and the regressed ($3\gamma_{\mathrm{avg,Pt}} - E_{\mathrm{adh}}$) value in the best-fit model, the $\gamma_{\mathrm{avg,Pt}}$ is 61 meV/Å^2. E_{adh} (and the regressed $\gamma_{\mathrm{avg,Pt}}$) could vary with temperature due to changes in hydroxylation, which would result in a change of E_{adh} with time in these simulations. If we assume the most extreme cases of full hydroxylation and full dehydroxylation of the silica surface, using the resulting new E_{adh} values (14 and 93 meV/Å^2, respectively) [83] give $\gamma_{\mathrm{avg,Pt}}$ of 58 meV/Å^2 and 84 meV/Å^2, respectively. Therefore, depending on the extent of hydroxylation, the effective $\gamma_{\mathrm{avg,Pt}}$ may vary between 58-84 meV/Å^2 but remains lower than the $\gamma_{\mathrm{avg,Pt}}$ in vacuum (96 meV/Å^2). The difference in surface energy between the range here (58-84 meV/Å^2) and Pt in vacuum (96 meV/Å^2) is likely due to a combination of stability imparted by zeolite encapsulation and (or) reduction in the surface energy via adsorbate binding, as suggested by Plessow et al. [61]. These results suggest that zeolite encapsulation slows down the rate of monomer formation in OR due to the lower $\gamma_{\mathrm{avg,Pt}}$. Consequently, zeolite encapsulation imparts additional stability for Pt nanoparticles in comparison to other common oxide supports.

4. Conclusions

Here, we used DFT calculations, thermodynamic correlations, and kMC simulations to develop free energy models that encompass the thermodynamic and kinetic parameters dictating the reversible interconversion between Pt nanoparticles and Pt^{2+} cations ion-exchanged in zeolites (predominantly Z_2Pt) in oxidizing and reducing environments. We employed two free energy models for Pt particles, supported and unsupported, to test their accuracy relative to experimental observations. Thermodynamic analyses of the structural transformation between Pt particles and Pt^{2+} cations in CHA over a variety of environmental conditions demonstrated similar conclusions from both free energy models. Consistent with the available experimental data for Pt particle redispersion for CHA in literature [2], we observed that most high temperature (> 600 K) and oxidizing conditions promote complete redispersion of Pt particles to ion-exchanged Pt^{2+}, while exposure to H_2 reduces cations to bulk Pt metal over a range of 550-923 K. Increasing H_2O pressures facilitates partial agglomeration of cations to Pt-oxide particles at temperatures < 723 K, which can influence the active site tunability and stability of Pt supported zeolites for different applications, such as the aftertreatment of exhaust gases [5,39,71,87–89]. Extending the thermodynamic predictions of both free energy models to other zeolite frameworks (BEA, MFI, and TON), we found that predictions were consistent with available experimental data for these zeolites, and that cationic Pt species are more favorable for zeolites with rings that expand upon ion-exchange. These results suggest that frameworks should be chosen according to the desired operating conditions and preferred Pt active site structure, and that knowledge of ion-exchange-induced ring expansions or contractions may aid in the selection of zeolite frameworks.

Next, we tested the accuracy of these different free energy models by simulating a kinetic redispersion mechanism via gas-phase mediated OR and the subsequent exchange of mobile PtO_2 (g) monomer species at the ion-exchange sites in the CHA zeolite. We used kMC simulations and determined the influence of $\bar{x}$, $s_{\bar{x}}$, $\gamma_{avg,Pt}$ (or $3\gamma_{avg,Pt} - E_{adh}$) and $\Delta G_{monomer}^{form}$ on model predictions, and our results suggest that the choice of initial particle size distribution and (or) adsorbates that influence particle surface energy influence the rate of ion-exchange and particle sintering during catalyst use. We found that the supported particle model has the best agreement with experimental data, and model results suggest that there is a stabilization effect imparted by the zeolite framework on encapsulated Pt particles. Therefore, this work provides a framework to select approximate free energy models for metal particles encapsulated in zeolites, simulate ion-exchange in other zeolite frameworks, and study the thermodynamics and kinetics of metal-containing zeolite catalysts under a variety of environmental conditions.

ASSOCIATED CONTENT

Supplementary information referred to in the main text (PDF)

Geometries of computed zeolite structures (ZIP)

Sample Python code for kinetic simulations (ZIP)

AUTHOR INFORMATION

Corresponding Author

*cp9wx@virginia.edu

Author Contributions

‡A.J. and A.W. contributed equally.

Funding Sources

This work was supported by the University of Virginia Double Hoo Research Grant and Gregory J. Canty Research Award, and the National Science Foundation Award Number 2144174-CBET.

ACKNOWLEDGMENT

The authors acknowledge financial support from the Double Hoo Research Grant (A.J., K.M.), Gregory J. Canty Research Award (A.J.), National Science Foundation Faculty Early Career Development Program Award Number 2144174-CBET (C.P., K.M., A.W.), and the U.S. Department of Energy, Office of Science, Office of Basic Energy Sciences, under Award Number DE-SC0019026 (R.G.) throughout the project. The authors also acknowledge the Research Computing at the University of Virginia for computational resources and technical support that contributed to the results presented in this publication.

References

[1] T. Wang, C. Ding, L. Ma, Z. Ma, M. Yang, J. Wang, K. Zhang, Redispersion of Pt nanoparticles encapsulated within ZSM-5 in oxygen and catalytic properties in partial oxidation of methane, J. Porous Mater. 29 (2022) 1337–1347. https://doi.org/10.1007/s10934-022-01250-0.

[2] M. Moliner, J.E. Gabay, C.E. Kliewer, R.T. Carr, J. Guzman, G.L. Casty, P. Serna, A. Corma, Reversible Transformation of Pt Nanoparticles into Single Atoms inside High-Silica Chabazite Zeolite, J. Am. Chem. Soc. 138 (2016) 15743–15750. https://doi.org/10.1021/jacs.6b10169.

[3] E. Fernández, L. Liu, M. Boronat, R. Arenal, P. Concepcion, A. Corma, Low-Temperature Catalytic NO Reduction with CO by Subnanometric Pt Clusters, ACS Catal. 9 (2019) 11530–11541. https://doi.org/10.1021/acscatal.9b03207.

[4] D. Hou, L. Grajciar, P. Nachtigall, C.J. Heard, Origin of the Unusual Stability of Zeolite-Encapsulated Sub-Nanometer Platinum, ACS Catal. 10 (2020) 11057–11068. https://doi.org/10.1021/acscatal.0c01344.

[5] L. Nie, D. Mei, H. Xiong, B. Peng, Z. Ren, X.I.P. Hernandez, A. DeLaRiva, M. Wang, M.H. Engelhard, L. Kovarik, A.K. Datye, Y. Wang, Activation of surface lattice oxygen in single-

atom Pt/CeO $_2$ for low-temperature CO oxidation, Science 358 (2017) 1419–1423. https://doi.org/10.1126/science.aao2109.

[6] C. Yin, F.R. Negreiros, G. Barcaro, A. Beniya, L. Sementa, E.C. Tyo, S. Bartling, K.-H. Meiwes-Broer, S. Seifert, H. Hirata, N. Isomura, S. Nigam, C. Majumder, Y. Watanabe, A. Fortunelli, S. Vajda, Alumina-supported sub-nanometer Pt10 clusters: amorphization and role of the support material in a highly active CO oxidation catalyst, J. Mater. Chem. A 5 (2017) 4923–4931. https://doi.org/10.1039/C6TA10989F.

[7] L. Lin, S. Yao, R. Gao, X. Liang, Q. Yu, Y. Deng, J. Liu, M. Peng, Z. Jiang, S. Li, Y.-W. Li, X.-D. Wen, W. Zhou, D. Ma, A highly CO-tolerant atomically dispersed Pt catalyst for chemoselective hydrogenation, Nat. Nanotechnol. 14 (2019) 354–361. https://doi.org/10.1038/s41565-019-0366-5.

[8] X. Deng, B. Qin, R. Liu, X. Qin, W. Dai, G. Wu, N. Guan, D. Ma, L. Li, Zeolite-Encaged Isolated Platinum Ions Enable Heterolytic Dihydrogen Activation and Selective Hydrogenations, J. Am. Chem. Soc. 143 (2021) 20898–20906. https://doi.org/10.1021/jacs.1c09535.

[9] M. Moliner, J. Gabay, C. Kliewer, P. Serna, A. Corma, Trapping of Metal Atoms and Metal Clusters by Chabazite under Severe Redox Stress, ACS Catal. 8 (2018) 9520–9528. https://doi.org/10.1021/acscatal.8b01717.

[10] L. Liu, M. Lopez-Haro, C.W. Lopes, C. Li, P. Concepcion, L. Simonelli, J.J. Calvino, A. Corma, Regioselective generation and reactivity control of subnanometric platinum clusters in zeolites for high-temperature catalysis, Nat. Mater. 18 (2019) 866–873. https://doi.org/10.1038/s41563-019-0412-6.

[11] X. Duan, X. Tian, J. Ke, Y. Yin, J. Zheng, J. Chen, Z. Cao, Z. Xie, Y. Yuan, Size controllable redispersion of sintered Au nanoparticles by using iodohydrocarbon and its implications, Chem. Sci. 7 (2016) 3181–3187. https://doi.org/10.1039/C5SC04283F.

[12] K. Morgan, A. Goguet, C. Hardacre, Metal Redispersion Strategies for Recycling of Supported Metal Catalysts: A Perspective, ACS Catal. 5 (2015) 3430–3445. https://doi.org/10.1021/acscatal.5b00535.

[13] S. Zhang, Y. Li, C. Ding, Y. Niu, Y. Zhang, B. Yang, G. Li, J. Wang, Z. Ma, L.-J. Yu, Atomic Dispersion of Pt Clusters Encapsulated Within ZSM-5 Depending on Aluminum Sites and Calcination Temperature, Small Struct. 4 (2023) 2200115. https://doi.org/10.1002/sstr.202200115.

[14] P. Tabib Zadeh Adibi, T. Pingel, E. Olsson, H. Grönbeck, C. Langhammer, Pt Nanoparticle Sintering and Redispersion on a Heterogeneous Nanostructured Support, J. Phys. Chem. C 120 (2016) 14918–14925. https://doi.org/10.1021/acs.jpcc.6b03874.

[15] M. Choi, Z. Wu, E. Iglesia, Mercaptosilane-Assisted Synthesis of Metal Clusters within Zeolites and Catalytic Consequences of Encapsulation, J. Am. Chem. Soc. 132 (2010) 9129–9137. https://doi.org/10.1021/ja102778e.

[16] L. Liu, A. Corma, Confining isolated atoms and clusters in crystalline porous materials for catalysis, Nat. Rev. Mater. 6 (2021) 244–263. https://doi.org/10.1038/s41578-020-00250-3.

[17] D. Hou, C.J. Heard, Migration of zeolite-encapsulated Pt and Au under reducing environments, Catal. Sci. Technol. 12 (2022) 1598–1609. https://doi.org/10.1039/D1CY02270A.

[18] J. Shan, M. Li, L.F. Allard, S. Lee, M. Flytzani-Stephanopoulos, Mild oxidation of methane to methanol or acetic acid on supported isolated rhodium catalysts, Nature 551 (2017) 605–608. https://doi.org/10.1038/nature24640.

[19] E. Peeters, I. Khalil, P. Eloy, S. Calderon-Ardila, J. Dijkmans, P. Ferrini, D.P. Debecker, R.A. Taylor, A.P. Douvalis, M. Dusselier, B.F. Sels, Tandem Reduction–Reoxidation Augments the Catalytic Activity of Sn-Beta Zeolites by Redispersion and Respeciation of SnO2 Clusters, Chem. Mater. 33 (2021) 9366–9381. https://doi.org/10.1021/acs.chemmater.1c03265.

[20] Y. Liu, Z. Li, Q. Yu, Y. Chen, Z. Chai, G. Zhao, S. Liu, W.-C. Cheong, Y. Pan, Q. Zhang, L. Gu, L. Zheng, Y. Wang, Y. Lu, D. Wang, C. Chen, Q. Peng, Y. Liu, L. Liu, J. Chen, Y. Li, A General Strategy for Fabricating Isolated Single Metal Atomic Site Catalysts in Y Zeolite, J. Am. Chem. Soc. 141 (2019) 9305–9311. https://doi.org/10.1021/jacs.9b02936.

[21] P. Serna, A. Rodríguez-Fernández, S. Yacob, C. Kliewer, M. Moliner, A. Corma, Single-Site vs. Cluster Catalysis in High Temperature Oxidations, Angew. Chem. 133 (2021) 16090–16098. https://doi.org/10.1002/ange.202102339.

[22] N. Felvey, J. Guo, R. Rana, L. Xu, S.R. Bare, B.C. Gates, A. Katz, A.R. Kulkarni, R.C. Runnebaum, C.X. Kronawitter, Interconversion of Atomically Dispersed Platinum Cations and Platinum Clusters in Zeolite ZSM-5 and Formation of Platinum *gem* -Dicarbonyls, J. Am. Chem. Soc. 144 (2022) 13874–13887. https://doi.org/10.1021/jacs.2c05386.

[23] E. Bello, V.J. Margarit, E.M. Gallego, F. Schuetze, C. Hengst, A. Corma, M. Moliner, Deactivation and regeneration studies on Pd-containing medium pore zeolites as passive NOx adsorbers (PNAs) in cold-start applications, Microporous Mesoporous Mater. 302 (2020) 110222. https://doi.org/10.1016/j.micromeso.2020.110222.

[24] Y. Ryou, J. Lee, S.J. Cho, H. Lee, C.H. Kim, D.H. Kim, Activation of Pd/SSZ-13 catalyst by hydrothermal aging treatment in passive NO adsorption performance at low temperature for cold start application, Appl. Catal. B Environ. 212 (2017) 140–149. https://doi.org/10.1016/j.apcatb.2017.04.077.

[25] Y. Ryou, J. Lee, H. Lee, C.H. Kim, D.H. Kim, Effect of various activation conditions on the low temperature NO adsorption performance of Pd/SSZ-13 passive NOx adsorber, Catal. Today 320 (2019) 175–180. https://doi.org/10.1016/j.cattod.2017.11.030.

[26] T.M. Lardinois, K. Mandal, V. Yadav, A. Wijerathne, B.K. Bolton, H. Lippie, C.W. Li, C. Paolucci, R. Gounder, Kinetic and Thermodynamic Factors Influencing Palladium Nanoparticle Redispersion into Mononuclear Pd(II) Cations in Zeolite Supports, J. Phys. Chem. C 126 (2022) 8337–8353. https://doi.org/10.1021/acs.jpcc.2c01613.

[27] T.M. Lardinois, J.S. Bates, H.H. Lippie, C.K. Russell, J.T. Miller, H.M.I. Meyer, K.A. Unocic, V. Prikhodko, X. Wei, C.K. Lambert, A.B. Getsoian, R. Gounder, Structural Interconversion between Agglomerated Palladium Domains and Mononuclear Pd(II) Cations in Chabazite Zeolites, Chem. Mater. 33 (2021) 1698–1713. https://doi.org/10.1021/acs.chemmater.0c04465.

[28] R. Ouyang, J.-X. Liu, W.-X. Li, Atomistic Theory of Ostwald Ripening and Disintegration of Supported Metal Particles under Reaction Conditions, J. Am. Chem. Soc. 135 (2013) 1760–1771. https://doi.org/10.1021/ja3087054.

[29] B.R. Goldsmith, E.D. Sanderson, R. Ouyang, W.-X. Li, CO- and NO-Induced Disintegration and Redispersion of Three-Way Catalysts Rhodium, Palladium, and Platinum: An ab Initio Thermodynamics Study, J. Phys. Chem. C 118 (2014) 9588–9597. https://doi.org/10.1021/jp502201f.

[30] E.D. Goodman, A.C. Johnston-Peck, E.M. Dietze, C.J. Wrasman, A.S. Hoffman, F. Abild-Pedersen, S.R. Bare, P.N. Plessow, M. Cargnello, Catalyst deactivation via decomposition

into single atoms and the role of metal loading, Nat. Catal. 2 (2019) 748–755. https://doi.org/10.1038/s41929-019-0328-1.

[31] J. Jones, H. Xiong, A.T. DeLaRiva, E.J. Peterson, H. Pham, S.R. Challa, G. Qi, S. Oh, M.H. Wiebenga, X.I. Pereira Hernández, Y. Wang, A.K. Datye, Thermally stable single-atom platinum-on-ceria catalysts via atom trapping, Science 353 (2016) 150–154. https://doi.org/10.1126/science.aaf8800.

[32] D. Kunwar, S. Zhou, A. DeLaRiva, E.J. Peterson, H. Xiong, X.I. Pereira-Hernández, S.C. Purdy, R. ter Veen, H.H. Brongersma, J.T. Miller, H. Hashiguchi, L. Kovarik, S. Lin, H. Guo, Y. Wang, A.K. Datye, Stabilizing High Metal Loadings of Thermally Stable Platinum Single Atoms on an Industrial Catalyst Support, ACS Catal. 9 (2019) 3978–3990. https://doi.org/10.1021/acscatal.8b04885.

[33] S.L. Hemmingson, C.T. Campbell, Trends in Adhesion Energies of Metal Nanoparticles on Oxide Surfaces: Understanding Support Effects in Catalysis and Nanotechnology, ACS Nano 11 (2017) 1196–1203. https://doi.org/10.1021/acsnano.6b07502.

[34] W. Sun, D.A. Kitchaev, D. Kramer, G. Ceder, Non-equilibrium crystallization pathways of manganese oxides in aqueous solution, Nat. Commun. 10 (2019) 573. https://doi.org/10.1038/s41467-019-08494-6.

[35] A. Shrestha, X. Gao, J.C. Hicks, C. Paolucci, Nanoparticle Size Effects on Phase Stability for Molybdenum and Tungsten Carbides, Chem. Mater. 33 (2021) 4606–4620. https://doi.org/10.1021/acs.chemmater.1c01120.

[36] G. Kresse, J. Furthmüller, Efficient iterative schemes for ab initio total-energy calculations using a plane-wave basis set, Phys. Rev. B 54 (1996) 11169–11186. https://doi.org/10.1103/PhysRevB.54.11169.

[37] P.E. Blöchl, Projector augmented-wave method, Phys. Rev. B 50 (1994) 17953–17979. https://doi.org/10.1103/PhysRevB.50.17953.

[38] G. Kresse, D. Joubert, From ultrasoft pseudopotentials to the projector augmented-wave method, Phys. Rev. B 59 (1999) 1758–1775. https://doi.org/10.1103/PhysRevB.59.1758.

[39] K. Mandal, Y. Gu, K.S. Westendorff, S. Li, J.A. Pihl, L.C. Grabow, W.S. Epling, C. Paolucci, Condition-Dependent Pd Speciation and NO Adsorption in Pd/Zeolites, ACS Catal. 10 (2020) 12801–12818. https://doi.org/10.1021/acscatal.0c03585.

[40] A. Jain, S.P. Ong, G. Hautier, W. Chen, W.D. Richards, S. Dacek, S. Cholia, D. Gunter, D. Skinner, G. Ceder, K.A. Persson, Commentary: The Materials Project: A materials genome approach to accelerating materials innovation, APL Mater. 1 (2013) 011002. https://doi.org/10.1063/1.4812323.

[41] J.P. Perdew, Y. Wang, Accurate and simple analytic representation of the electron-gas correlation energy, Phys. Rev. B 45 (1992) 13244–13249. https://doi.org/10.1103/PhysRevB.45.13244.

[42] S. Grimme, J. Antony, S. Ehrlich, H. Krieg, A consistent and accurate ab initio parametrization of density functional dispersion correction (DFT-D) for the 94 elements H-Pu, J. Chem. Phys. 132 (2010) 154104. https://doi.org/10.1063/1.3382344.

[43] S. Grimme, S. Ehrlich, L. Goerigk, Effect of the damping function in dispersion corrected density functional theory, J. Comput. Chem. 32 (2011) 1456–1465. https://doi.org/10.1002/jcc.21759.

[44] J. Heyd, G.E. Scuseria, M. Ernzerhof, Hybrid functionals based on a screened Coulomb potential, J. Chem. Phys. 118 (2003) 8207–8215. https://doi.org/10.1063/1.1564060.

[45] J. Heyd, G.E. Scuseria, Efficient hybrid density functional calculations in solids: Assessment of the Heyd–Scuseria–Ernzerhof screened Coulomb hybrid functional, J. Chem. Phys. 121 (2004) 1187–1192. https://doi.org/10.1063/1.1760074.

[46] A.V. Krukau, O.A. Vydrov, A.F. Izmaylov, G.E. Scuseria, Influence of the exchange screening parameter on the performance of screened hybrid functionals, J. Chem. Phys. 125 (2006) 224106. https://doi.org/10.1063/1.2404663.

[47] C.T. Campbell, J.R.V. Sellers, The Entropies of Adsorbed Molecules, J. Am. Chem. Soc. 134 (2012) 18109–18115. https://doi.org/10.1021/ja3080117.

[48] H. Li, C. Paolucci, W.F. Schneider, Zeolite Adsorption Free Energies from ab Initio Potentials of Mean Force, J. Chem. Theory Comput. 14 (2018) 929–938. https://doi.org/10.1021/acs.jctc.7b00716.

[49] M.W. Penninger, C.H. Kim, L.T. Thompson, W.F. Schneider, DFT Analysis of NO Oxidation Intermediates on Undoped and Doped LaCoO3 Perovskite, J. Phys. Chem. C 119 (2015) 20488–20494. https://doi.org/10.1021/acs.jpcc.5b06351.

[50] A. Asthagiri, M. Janik, Computational Catalysis, Royal Society of Chemistry, 2014.

[51] M.W. Chase, C.A. Davies, J.R. Downey, D.J. Frurip, R.A. McDonald, A.N. Syverud, NIST-JANAF Thermochemical Tables, NIST Stand. Ref. Database 13 (1985). https://janaf.nist.gov/janbanr.html (accessed January 15, 2024).

[52] S.P. Ong, W.D. Richards, A. Jain, G. Hautier, M. Kocher, S. Cholia, D. Gunter, V.L. Chevrier, K.A. Persson, G. Ceder, Python Materials Genomics (pymatgen): A robust, open-source python library for materials analysis, Comput. Mater. Sci. 68 (2013) 314–319. https://doi.org/10.1016/j.commatsci.2012.10.028.

[53] R. Tran, Z. Xu, B. Radhakrishnan, D. Winston, W. Sun, K.A. Persson, S.P. Ong, Surface energies of elemental crystals, Sci. Data 3 (2016) 160080. https://doi.org/10.1038/sdata.2016.80.

[54] W. Sun, G. Ceder, Efficient creation and convergence of surface slabs, Surf. Sci. 617 (2013) 53–59. https://doi.org/10.1016/j.susc.2013.05.016.

[55] D.S. Sholl, J.A. Steckel, Density Functional Theory: A Practical Introduction, John Wiley & Sons, 2022.

[56] G. Wulff, XXV. Zur Frage der Geschwindigkeit des Wachsthums und der Auflösung der Krystallflächen, Z. Für Krist. - Cryst. Mater. 34 (1901) 449–530. https://doi.org/10.1524/zkri.1901.34.1.449.

[57] M.J. Ungerer, D. Santos-Carballal, A. Cadi-Essadek, C.G.C.E. van Sittert, N.H. de Leeuw, Interaction of H2O with the Platinum Pt (001), (011), and (111) Surfaces: A Density Functional Theory Study with Long-Range Dispersion Corrections, J. Phys. Chem. C 123 (2019) 27465–27476. https://doi.org/10.1021/acs.jpcc.9b06136.

[58] Z. Mao, C.T. Campbell, Predicting a Key Catalyst-Performance Descriptor for Supported Metal Nanoparticles: Metal Chemical Potential, ACS Catal. 11 (2021) 8284–8291. https://doi.org/10.1021/acscatal.1c01870.

[59] C.T. Campbell, Z. Mao, Chemical Potential of Metal Atoms in Supported Nanoparticles: Dependence upon Particle Size and Support, ACS Catal. 7 (2017) 8460–8466. https://doi.org/10.1021/acscatal.7b03090.

[60] S.K. Ignatov, A.G. Razuvaev, A.S. Loginova, A.E. Masunov, Global Structure Optimization of Pt Clusters Based on the Modified Empirical Potentials, Calibrated using Density Functional Theory, J. Phys. Chem. C 123 (2019) 29024–29036. https://doi.org/10.1021/acs.jpcc.9b08691.

[61] P.N. Plessow, F. Abild-Pedersen, Sintering of Pt Nanoparticles via Volatile PtO $_2$: Simulation and Comparison with Experiments, ACS Catal. 6 (2016) 7098–7108. https://doi.org/10.1021/acscatal.6b01646.

[62] F. Grillo, H. Van Bui, J.A. Moulijn, M.T. Kreutzer, J.R. Van Ommen, Understanding and Controlling the Aggregative Growth of Platinum Nanoparticles in Atomic Layer Deposition: An Avenue to Size Selection, J. Phys. Chem. Lett. 8 (2017) 975–983. https://doi.org/10.1021/acs.jpclett.6b02978.

[63] J. de Graaf, A.J. van Dillen, K.P. de Jong, D.C. Koningsberger, Preparation of Highly Dispersed Pt Particles in Zeolite Y with a Narrow Particle Size Distribution: Characterization by Hydrogen Chemisorption, TEM, EXAFS Spectroscopy, and Particle Modeling, J. Catal. 203 (2001) 307–321. https://doi.org/10.1006/jcat.2001.3337.

[64] J. Doke, GRABIT, MATLAB Cent. File Exch. (2023). https://www.mathworks.com/matlabcentral/fileexchange/7173-grabit (accessed March 28, 2023).

[65] A.A. Hagberg, D.A. Schult, P.J. Swart, Exploring Network Structure, Dynamics, and Function using NetworkX, (2008).

[66] A. Wijerathne, A. Sawyer, R. Daya, C. Paolucci, Competition between Mononuclear and Binuclear Copper Sites across Different Zeolite Topologies, JACS Au 4 (2024) 197–215. https://doi.org/10.1021/jacsau.3c00632.

[67] W. Loewenstein, The distribution of aluminum in the tetrahedra of silicates and aluminates, Am. Mineral. 39 (1954) 92–96.

[68] R.G. Bell, R.A. Jackson, C.R.A. Catlow, Löwenstein’s rule in zeolite A: A computational study, Zeolites 12 (1992) 870–871. https://doi.org/10.1016/0144-2449(92)90065-W.

[69] S. Li, H. Li, R. Gounder, A. Debellis, I.B. Müller, S. Prasad, A. Moini, W.F. Schneider, First-Principles Comparison of Proton and Divalent Copper Cation Exchange Energy Landscapes in SSZ-13 Zeolite, J. Phys. Chem. C 122 (2018) 23564–23573. https://doi.org/10.1021/acs.jpcc.8b07213.

[70] K. Muraoka, W. Chaikittisilp, T. Okubo, Energy Analysis of Aluminosilicate Zeolites with Comprehensive Ranges of Framework Topologies, Chemical Compositions, and Aluminum Distributions, J. Am. Chem. Soc. 138 (2016) 6184–6193. https://doi.org/10.1021/jacs.6b01341.

[71] C. Paolucci, A.A. Parekh, I. Khurana, J.R. Di Iorio, H. Li, J.D. Albarracin Caballero, A.J. Shih, T. Anggara, W.N. Delgass, J.T. Miller, F.H. Ribeiro, R. Gounder, W.F. Schneider, Catalysis in a Cage: Condition-Dependent Speciation and Dynamics of Exchanged Cu Cations in SSZ-13 Zeolites, J. Am. Chem. Soc. 138 (2016) 6028–6048. https://doi.org/10.1021/jacs.6b02651.

[72] L.K. Ono, B. Yuan, H. Heinrich, B.R. Cuenya, Formation and Thermal Stability of Platinum Oxides on Size-Selected Platinum Nanoparticles: Support Effects, J. Phys. Chem. C 114 (2010) 22119–22133. https://doi.org/10.1021/jp1086703.

[73] Y. Xu, W.A. Shelton, W.F. Schneider, Effect of Particle Size on the Oxidizability of Platinum Clusters, J. Phys. Chem. A 110 (2006) 5839–5846. https://doi.org/10.1021/jp0547111.

[74] R.K. Nomiyama, M.J. Piotrowski, J.L.F. Da Silva, Bulk structures of PtO and PtO 2 from density functional calculations, Phys. Rev. B 84 (2011) 100101. https://doi.org/10.1103/PhysRevB.84.100101.

[75] M. Taleblou, M.F. Camellone, S. Fabris, S. Piccinin, Oxidation of Gas-Phase and Supported Pt Nanoclusters: An *Ab Initio* Investigation, J. Phys. Chem. C 126 (2022) 10880–10888. https://doi.org/10.1021/acs.jpcc.2c02176.

[76] Y. Chai, W. Shang, W. Li, G. Wu, W. Dai, N. Guan, L. Li, Noble Metal Particles Confined in Zeolites: Synthesis, Characterization, and Applications, Adv. Sci. 6 (2019) 1900299. https://doi.org/10.1002/advs.201900299.

[77] L. Liu, M. Lopez-Haro, J.A. Perez-Omil, M. Boronat, J.J. Calvino, A. Corma, Direct assessment of confinement effect in zeolite-encapsulated subnanometric metal species, Nat. Commun. 13 (2022) 821. https://doi.org/10.1038/s41467-022-28356-y.

[78] K.D. Hammonds, V. Heine, M.T. Dove, Rigid-Unit Modes and the Quantitative Determination of the Flexibility Possessed by Zeolite Frameworks, J. Phys. Chem. B 102 (1998) 1759–1767. https://doi.org/10.1021/jp980006z.

[79] W. Masierak, T. Emmler, G. Buntkowsky, A. Gutsze, Influence of Cation Exchange on the 27Al-NMR Spectra of Zeolites, Z. Für Phys. Chem. 217 (2003) 1613–1626. https://doi.org/10.1524/zpch.217.12.1613.20478.

[80] P. Wynblatt, N.A. Gjostein, Particle growth in model supported metal catalysts—I. Theory, Acta Metall. 24 (1976) 1165–1174. https://doi.org/10.1016/0001-6160(76)90034-1.

[81] P.N. Plessow, C.T. Campbell, Influence of Adhesion on the Chemical Potential of Supported Nanoparticles as Modeled with Spherical Caps, ACS Catal. 12 (2022) 2302–2308. https://doi.org/10.1021/acscatal.1c04633.

[82] M.D. Hall, G.J. Foran, M. Zhang, P.J. Beale, T.W. Hambley, XANES Determination of the Platinum Oxidation State Distribution in Cancer Cells Treated with Platinum(IV) Anticancer Agents, J. Am. Chem. Soc. 125 (2003) 7524–7525. https://doi.org/10.1021/ja0354770.

[83] P.N. Plessow, R.S. Sánchez-Carrera, L. Li, M. Rieger, S. Sauer, A. Schaefer, F. Abild-Pedersen, Modeling the Interface of Platinum and α-Quartz(001): Implications for Sintering, J. Phys. Chem. C 120 (2016) 10340–10350. https://doi.org/10.1021/acs.jpcc.6b01403.

[84] H.-L.T. Le, J. Goniakowski, C. Noguera, A. Koltsov, J.-M. Mataigne, Effects of surface hydroxylation on adhesion at zinc/silica interfaces, Phys. Chem. Chem. Phys. 20 (2018) 15581–15588. https://doi.org/10.1039/C8CP02139B.

[85] R. Ferreira de Morais, A.A. Franco, P. Sautet, D. Loffreda, Interplay between Reaction Mechanism and Hydroxyl Species for Water Formation on Pt(111), ACS Catal. 5 (2015) 1068–1077. https://doi.org/10.1021/cs5012525.

[86] W. Lew, M.C. Crowe, E. Karp, O. Lytken, J.A. Farmer, L. Árnadóttir, C. Schoenbaum, C.T. Campbell, The Energy of Adsorbed Hydroxyl on Pt(111) by Microcalorimetry, J. Phys. Chem. C 115 (2011) 11586–11594. https://doi.org/10.1021/jp201632t.

[87] C. Paolucci, I. Khurana, A.A. Parekh, S. Li, A.J. Shih, H. Li, J.R. Di Iorio, J.D. Albarracin-Caballero, A. Yezerets, J.T. Miller, W.N. Delgass, F.H. Ribeiro, W.F. Schneider, R. Gounder, Dynamic multinuclear sites formed by mobilized copper ions in NO $_x$ selective catalytic reduction, Science 357 (2017) 898–903. https://doi.org/10.1126/science.aan5630.

[88] L. Chen, H. Falsig, T.V.W. Janssens, J. Jansson, M. Skoglundh, H. Grönbeck, Effect of Al-distribution on oxygen activation over Cu–CHA, Catal. Sci. Technol. 8 (2018) 2131–2136. https://doi.org/10.1039/C8CY00083B.

[89] F. Gao, D. Mei, Y. Wang, J. Szanyi, C.H.F. Peden, Selective Catalytic Reduction over Cu/SSZ-13: Linking Homo- and Heterogeneous Catalysis, J. Am. Chem. Soc. 139 (2017) 4935–4942. https://doi.org/10.1021/jacs.7b01128.